ACS OMEGA

Open Access

http://pubs.acs.org/journal/acsodf

Article

Enhanced Delivery and Potency of Chemotherapeutics in Melanoma Treatment via Magnetite Nanobioconjugates

Erika Díaz,[‖] Valentina Quezada,[‖] Javier Cifuentes, Nydia Yadira Arias Morales, Luis H. Reyes, Carolina Muñoz-Camargo, and Juan C. Cruz*

Cite This: *ACS Omega* 2024, 9, 45402−45420

Read Online

ACCESS | Metrics & More | Article Recommendations | Supporting Information

ABSTRACT: Melanoma, known for its aggressive metastatic potential, poses significant treatment challenges. Despite the potent antiproliferative effects of anticancer drugs, systemic toxicity and low water solubility limit their efficacy. This study addresses these challenges by employing magnetite (Fe_3O_4) nanobioconjugates as a drug delivery system, aimed at enhancing drug solubility and reducing off-target effects in melanoma therapy. Magnetite nanoparticles (MNPs) were engineered with functional molecules and loaded with the anticancer agents Temozolomide (TMZ) or paclitaxel (PTX). The nanobioconjugates were characterized via Fourier transform infrared spectroscopy (FTIR), thermogravimetric analysis (TGA), dynamic light scattering (DLS), and transmission electron microscopy (TEM). The results validated the efficacious synthesis and drug loading, attaining efficiencies ranging from 32 to 72% for TMZ and 32 to 60% for PTX. Biocompatibility assessments demonstrated excellent tolerance, with minimal hemolysis rates and platelet aggregation. In vitro studies revealed enhanced cytotoxicity against A-375 human melanoma cells compared to free drugs, with cellular uptake facilitated primarily through macropinocytosis, caveolin-, and clathrin-mediated endocytosis. Furthermore, the nanobioconjugates exhibited significant efficacy in targeting A-375 melanoma spheroids, underlining their potential in melanoma therapy. This research underscores magnetite nanobioconjugates as a promising avenue for targeted melanoma treatment, offering enhanced drug delivery specificity and reduced systemic toxicity in oncological drug delivery systems.

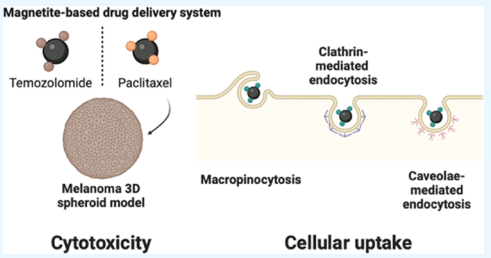

1. INTRODUCTION

Melanoma is a type of cancer that originates in melanocytes, the cells responsible for producing melanin, which are found within the basal layer of the epidermis. It ranks as the sixth most commonly diagnosed cancer and accounts for an alarming 80% of deaths related to skin cancer.[1,2] Traditional therapeutic methods remain integral in treating approximately half of all cancer patients. Chemotherapy, whether used alone or in combination with other treatments, continues to be the predominant cancer therapy, contributing to improved survival rates.[3] However, the use of anticancer drugs presents significant challenges. While these agents target tumor cells, they can also damage surrounding healthy tissues, resulting in numerous side effects that can undermine the treatment's efficacy.[4,5] Common side effects include neuropathies, bone marrow suppression, gastrointestinal issues, skin conditions, hair loss, and fatigue.[6] Despite breakthroughs in cancer research and therapeutic methodologies, managing melanoma remains a significant challenge. This is primarily due to its aggressive nature, potential for metastasis, and inherent resistance to standard chemotherapeutic drugs.[7]

Paclitaxel (PTX) and Temozolomide (TMZ) are two widely used chemotherapeutic agents. PTX promotes the assembly of tubulin into microtubules and prevents their dissociation, thereby blocking cell cycle progression, preventing mitosis, and inhibiting cancer cell growth.[8] In contrast, TMZ works by methylating DNA, resulting in inhibited DNA and cellular replication.[9] Despite their potent antiproliferative effects, these drugs have significant drawbacks, including systemic toxicity due to nonselective distribution to normal cells and low water solubility, which have been a persistent clinical hurdle.[10]

Nanotechnology has made significant advances in improving the bioavailability of hydrophobic drugs, reducing drug degradation, and enabling sustained and triggered release. As drug carriers, nanomaterials offer targeted tumor delivery, the capacity to bind or hold numerous drug molecules, and the ability to overcome solubility and stability issues, thereby prolonging the circulation half-life of the drug.[2,11−13] They also leverage the enhanced permeability and retention (EPR) effect at the tumor site. This EPR effect, resulting from the tumor's abnormal vasculature and permeable blood vessels, facilitates passive targeting of nanoparticles, ensuring increased drug

Received: August 12, 2024
Revised: September 29, 2024
Accepted: October 4, 2024
Published: October 30, 2024

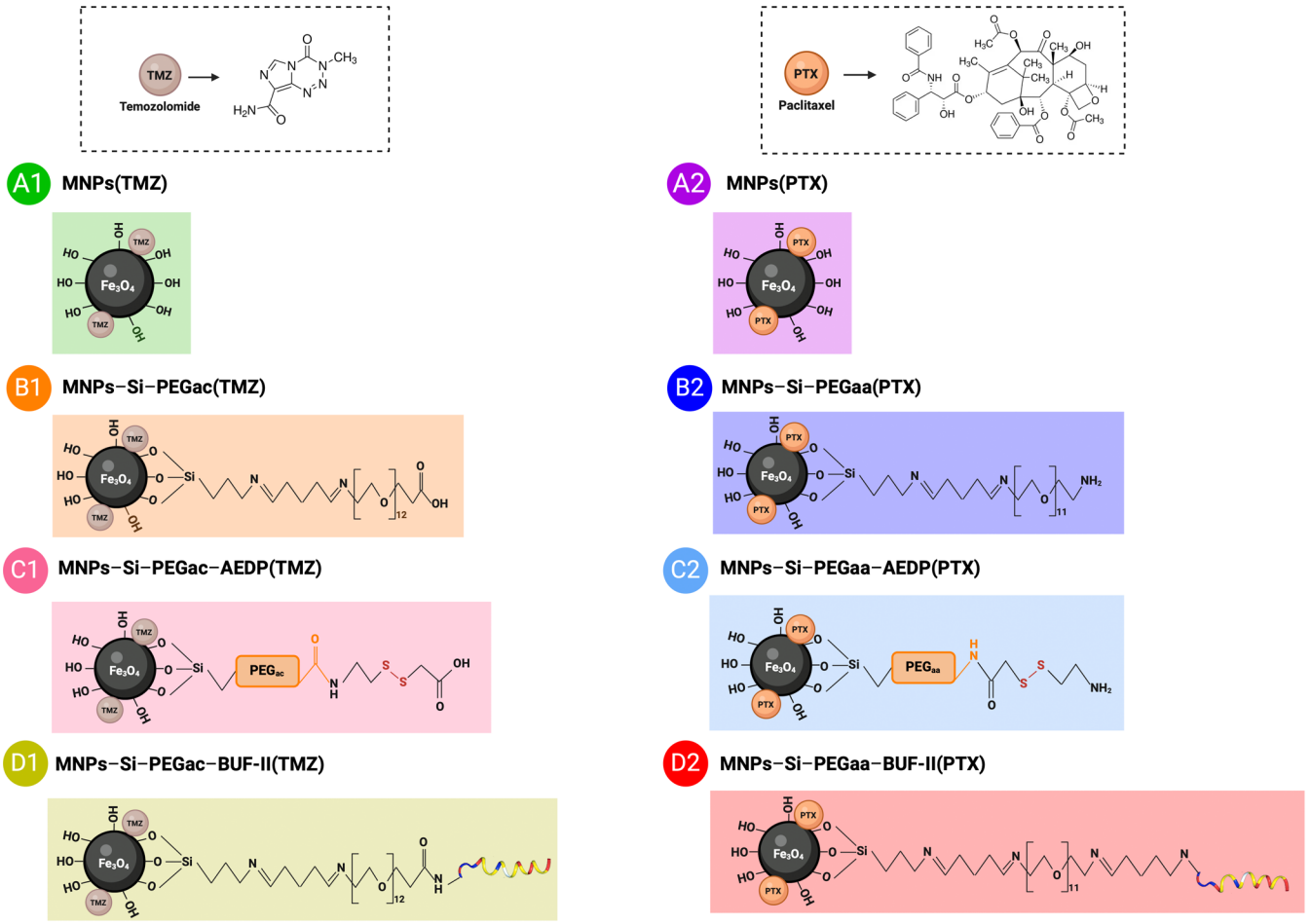

Figure 1. Final chemical structures of the evaluated nanobioconjugates. Drug loading on (A) bare MNPs (control), (B) PEGylated MNPs, (C) AEDP–PEGylated MNPs, and (D) BUF-II–PEGylated MNPs. Created with BioRender.com.

delivery to the tumor while minimizing exposure to healthy tissues.[2,14]

Among various nanomaterials, such as liposomes, nanoparticles, dendrimers, and micelles[15] magnetic iron oxide nanoparticles (IONPs) are among the most useful metal nanoparticles in multiple fields, especially in biomedical applications.[16,17] Characterized by their magnetic properties, biocompatibility, stability, and biodegradability, magnetic nanoparticles offer a high surface area-to-volume ratio, enabling efficient drug loading. Their easy functionalization with various targeting ligands and biomolecules can ensure precise delivery to cancer cells. Moreover, their magnetic nature allows for manipulation using external magnetic fields, further enhancing tumor targeting.[18,19] It has been demonstrated that IONPs can enhance drug absorption, reduce drug toxicity, and mitigate drug resistance.[20] Recent research has highlighted the potential of IONPs as pH-responsive nanoplatforms to enhance pancreatic cancer treatment,[21] facilitate magnetic drug targeting for the effective delivery of phytochemicals in cancer therapy,[22] and serve as a trimodal synergistic strategy for photothermal-chemodynamic-coordinated chemotherapy.[23] Additionally, IONPs exhibit remarkable capabilities in hyperthermia, magnetic resonance imaging, and surface-enhanced Raman scattering for advanced imaging and diagnostics.[24]

A majority of approaches have focused on loading PTX or TMZ onto nanoparticles for melanoma treatment due to the challenges in creating stable covalent immobilization of these drugs on the nanoparticles' surfaces.[25−27] Among these nanocarriers, polymeric-coated magnetic nanoparticles have been of particular interest, as the coating does not interfere with their magnetic properties.[28] This advantage can be utilized to enhance tumor targeting with the aid of external magnetic fields[29] or in combined photothermal and photodynamic therapy.[30,31]

Magnetite (Fe_3O_4) nanoparticles (MNPs), the most widely used IONPs in biomedical applications,[32,33] are favored for their superparamagnetic behavior at room temperature and high saturation magnetization.[34] These nanoparticles can be easily synthesized by the chemical coprecipitation method, which involves using an aqueous iron salt (Fe^{2+} and Fe^{3+}) solution and adding a strong basic solution under an inert atmosphere at room temperature. The advantages of this method include the absence of toxic intermediates or solvents and no requirement for precursor complexes.[35]

This study proposes the design and *in vitro* evaluation of magnetite nanoparticle candidates for melanoma treatment by loading PTX or TMZ onto PEGylated nanoconjugates, incorporating either a multifunctional peptide or a reducible disulfide linker. The objective is to assess the impact of these molecules on drug loading efficiency and evaluate the nanobioconjugates' effectiveness against human melanoma cells. The use of polyethylene glycol (PEG) is driven by its well-known ability to reduce opsonization due to its un-

https://doi.org/10.1021/acsomega.4c07415
ACS Omega 2024, 9, 45402−45420

charged, hydrophilic, and nonimmunogenic properties.[36,37] The presence of PEG chains on the nanoparticle surface has been shown to enhance both their colloidal stability in aqueous suspension[38] and their blood half-life *in vivo*[5,39] Moreover, the antibacterial peptide Buforin II (BUF-II) among its translocating capabilities[40] has also proved to have cancer-selective cytotoxicity.[41,42] Studies have shown that BUF-II interacts with gangliosides in cancer cells.[41] The use of this peptide allows for the creation of nanobioconjugates with high endosome release efficiency and cytosolic accumulation in various cell lines,[43,44] while also increasing their affinity for cancer cells. The addition of a reducible disulfide linker was also evaluated, as previous studies have reported that it enhances the translocation capabilities of nanobioconjugates.[45,46]

This paper will delve into the synthesis, physicochemical, and biological characterization of these nanobioconjugates, assessing their drug loading efficiency, thermal stability, morphology, biocompatibility, cytotoxicity, and internalization pathways in both cancerous and noncancerous cell lines. The research aims to elucidate the multifunctionality of these nanobioconjugates, combined with the EPR effect, paving the way for future therapeutic applications.

2. MATERIALS AND METHODS

2.1. Synthesis and Functionalization of MNPs. MNPs were synthesized using the chemical coprecipitation method. Initially, 0.01 mol of iron(II) chloride tetrahydrate ($FeCl_2$) and 0.02 mol of iron(III) chloride hexahydrate ($FeCl_3$) were solubilized in 100 mL of type I water. This solution was then homogenized and cooled to 2 °C. Simultaneously, 0.08 mol of NaOH was dissolved in 100 mL of type I water and also cooled to 2 °C. The iron chlorides solution was magnetically stirred at 300 rpm in a sealed round-bottom flask while nitrogen gas was bubbled through to desorb oxygen and prevent oxidation. After 10 min, NaOH solution was added dropwise at a 5 mL/min rate with constant stirring and a continuous nitrogen flow. A black precipitate formed, indicating the creation of MNPs. After the addition of NaOH was complete, the magnetite solution was stirred for another hour at 300 rpm under a continuous nitrogen flow. The MNPs were washed three times with a 1.5% (w/v) NaCl solution and twice with type I water. A neodymium magnet was used to facilitate nanoparticle precipitation between washes, and sonication was applied at 40 kHz frequency and 38% amplitude during the washing steps.

After synthesis, the yield of the MNPs was measured. A 100 mg sample of MNPs was resuspended in 40 mL of type I water and sonicated for 10 min at a frequency of 40 kHz and an amplitude of 38%. Then, 250 μL of TBAH was added, and the mixture was sonicated for 1 min and magnetically stirred for 3 min. Subsequently, 50 μL of glacial acetic acid was added, followed by another round of sonication for 1 min and stirring for 3 min. Finally, 1 mL of a 20% (v/v) APTES solution was gradually added to the MNPs, and the reaction was maintained at 60 °C with constant stirring at 200 rpm for 1 h. The silanized nanoparticles were then washed as previously described and stored at 4 °C until further use.

2.2. Synthesis of Nanobioconjugates. For all immobilizations, amine−amine conjugation was assessed using the cross-linker glutaraldehyde, resulting in the formation of imine bonds. Amine-carboxyl conjugation was assessed using zero-length cross-linkers EDC/NHS, leading to the formation of amide bonds. The final structures of the evaluated nanobioconjugates are depicted in Figure 1.

2.2.1. PEGylation of Silanized MNPs. To achieve PEGylation of the MNPs, 100 mg of the silanized nanoparticles were first resuspended in 40 mL of type I water. This mixture was sonicated for 10 min, utilizing a frequency of 40 kHz and an amplitude of 38%. Next, 2 mL of a 2% (v/v) glutaraldehyde solution was added to the MNPs mixture, and the solution was stirred at 250 rpm for 1 h. Subsequently, 10 mg of NH_2−PEG_{12}-NH_2 (PEGaa) or NH_2−PEG_{12}-propionic acid (PEGac) were dissolved in 5 mL of type I water and added to the nanoparticle solution. The reaction was allowed to proceed for 24 h, with the solution being maintained under mechanical agitation at 250 rpm. Finally, the obtained PEGylated MNPs were washed and stored as previously described.

2.2.2. AEDP Immobilization on PEGylated MNPs. The immobilization of AEDP on PEGylated (PEGac) nanoparticles was initiated by dissolving 14 mg of EDC and 7 mg of NHS in 5 mL of type I water. This solution was then added to 100 mg of PEGylated MNPs, which had been preresuspended in 40 mL of type I water. The mixture was subjected to constant stirring at a rate of 250 rpm for 15 min. After this, 5 mg of AEDP was incorporated into the solution. For the immobilization of AEDP on the PEGylated (PEGaa) nanoparticles, 5 mg of AEDP was added to the activating solution of EDC and NHS and allowed to react under constant stirring at 250 rpm for 15 min. This activated AEDP solution was then added to 100 mg of the PEGylated nanoparticles. In both cases, the reaction was allowed to proceed for 24 h, maintained under mechanical agitation at 250 rpm. The obtained PEGylated−AEDP nanoparticles were washed and stored as previously described.

2.2.3. Immobilization of BUF-II on PEGylated MNPs. The amine terminal of BUF-II was conjugated to the free amine group of the PEGaa or the carboxyl group of the PEGac of the preliminary nanobioconjugates. To initiate this process, 100 mg of PEGylated nanoparticles were resuspended in 40 mL of type I water and subjected to sonication for 10 min, utilizing a frequency of 40 kHz and an amplitude of 38%. Fourteen mg of EDC and 7 mg of NHS were dissolved in 5 mL of type I water. This solution was subsequently added to the free amine PEGylated nanoparticles and subjected to constant stirring at a rate of 250 rpm for a duration of 15 min. In the case of immobilization by the carboxyl group, 2 mL of a 2% (v/v) glutaraldehyde solution was added to the PEGylated nanoparticle mixture and maintained under stirring at 250 rpm for 1 h. Next, 1 mL of BUF-II at a concentration of 1 mg/mL was incorporated into the solution. The reaction was allowed to proceed for 24 h, maintained under mechanical agitation at 250 rpm. The obtained PEGylated−BUF-II nanoparticles were washed and stored as previously described.

2.2.4. Drug Loading on PEGylated Nanobioconjugates. 100 mg of bare nanoparticles (as a control), PEGylated nanoparticles, PEGylated−AEDP nanoparticles, or PEGylated−BUF-II nanoparticles were resuspended in 40 mL of type I water and sonicated for 10 min at a frequency of 40 kHz and an amplitude of 38%. Then, 5 mg of TMZ or PTX were diluted in 1 mL of DMSO, added to the MNPs solution, and left under stirring at 250 rpm for 24 h. The final nanobioconjugates were washed and stored as previously described.

2.3. Drug Loading Efficiency. The drug loading content on the MNPs was determined as described in a previous study,[47] utilizing the intermediate nanobioconjugates. The

https://doi.org/10.1021/acsomega.4c07415
ACS Omega 2024, 9, 45402−45420

drug loading efficiency was calculated using eq 1, where the amount of drug loaded corresponds to the previously determined drug loading content, and the amount of drug used refers to the total amount of drug initially added.

$$\text{drug loading efficiency (\%)} = \frac{\text{amount of drug loaded}}{\text{amount of drug used}} \times 100 \quad (1)$$

2.4. Biocompatibility Studies. The biocompatibility of the synthesized nanobioconjugates was evaluated by assessing their cytotoxic, hemolytic, and platelet aggregation potential.

2.4.1. Hemolysis. Hemocompatibility was evaluated according to the ISO 10993-4:2018 standard. Blood samples were collected from a healthy human donor into a vacutainer tube with EDTA (collected with permission from the ethics committee at Universidad de Los Andes, minute number 928-2018. The study recruitment started on October 12, 2022, and ended on January 8, 2023. Participants gave informed written consent between January 10, 2023, and October 10, 2023). Erythrocytes were isolated by centrifugation at 1800 rpm for 15 min. After discarding the supernatant, the erythrocytes were washed three times with PBS 1X. To prepare a stock solution, 2 mL of the washed erythrocytes (4.5×10^6 erythrocytes/μL) were suspended in 18 mL of PBS 1X and carefully homogenized. The nanobioconjugates were tested at serial dilutions from 100 to 6.25 μg/mL in PBS 1X. Triton X-100 (10% v/v) and PBS 1X were used as the positive and negative controls, respectively. To evaluate the hemolytic activity, 100 μL of each treatment were seeded with 100 μL of the erythrocyte stock solution in a 96-well microplate. After incubation at 37 °C with 5% CO_2 for 1 h, the plate was centrifuged at 1800 rpm for 5 min. Then, 100 μL of the supernatants were transferred to another 96-well plate. Finally, absorbance was read at 450 nm in a microplate reader (Multiskan FC Microplate Photometer, Thermo Fisher Scientific, MA), and hemolysis percentage was calculated by eq 2. A_S, A_{C-}, A_{C+} are the absorbances of the sample, negative control and positive control, respectively.

$$\text{hemolysis (\%)} = \frac{A_S - A_{C-}}{A_{C+} - A_{C-}} \times 100 \quad (2)$$

2.4.2. Platelet Aggregation Assay. The platelet aggregation assay was conducted following the ISO 10993-4:2018 standard. Blood samples were collected from a healthy human donor into a vacutainer tube containing sodium citrate (collected with permission from the ethics committee at Universidad de Los Andes, minute number 928-2018. The study recruitment started on October 12, 2022, and ended on January 8, 2023. Participants gave informed written consent between January 10, 2023, and October 10, 2023). Platelet-rich plasma (PRP) was obtained by centrifuging the blood samples at 1000 rpm for 15 min at room temperature. The erythrocytes were discarded, and the supernatant containing PRP was used for the assay. The nanobioconjugates were tested at serial dilutions ranging from 100 μg/mL to 6.25 μg/mL. Thrombin (9U) and PBS 1X were used as the positive and negative controls, respectively. The aggregation capacity was evaluated by exposing 50 μL of PRP to 50 μL of the different treatments in a 96-well microplate. After incubating at 37 °C for 5 min, absorbance was measured at 620 nm in a microplate reader (Multiskan FC Microplate Photometer, Thermo Fisher Scientific, MA, USA). The platelet aggregation percentage was calculated by eq 3. A_S and A_{C+} are the absorbances of the sample and positive control, respectively.

$$\text{platelet aggregation (\%)} = \frac{A_S}{A_{C+}} \times 100 \quad (3)$$

2.4.3. Cytotoxicity. To identify the nanobioconjugates with the highest potential for drug delivery in melanoma treatment, cytotoxicity tests were performed. The cytocompatibility of the nanobioconjugates, loaded with either PTX or TMZ, was evaluated based on their effect on the plasma membrane integrity of HaCaT keratinocytes (CVCL_0038) and human melanoma cells A-375 (CRL-1619). This was done using a colorimetric assay to quantify the lactate dehydrogenase enzyme (LDH), employing a commercial LDH-Cytotoxicity assay kit. The nanobioconjugates were tested in 1:2 serial dilutions from 100 μg/mL to 6.25 μg/mL. Additionally, free TMZ and free PTX, previously diluted in DMSO (10 mg/mL), were evaluated across 5 serial dilutions, assuming a 15% (w/w) drug adsorption on the nanoparticles at the highest concentration (100 μg/mL). Triton X-100 (1% v/v)-treated cells medium served as positive control, while nonexposed cells medium served as negative control. Initially, 100 μL of a cell stock solution in DMEM medium supplemented with 10% FBS (v/v) was seeded in a 96-well microplate. The seeding density was 1×10^4 cells/well for both HaCaT and A-375 cells. After incubating in a humidified atmosphere at 37 °C with 5% CO_2 for 24 h, the medium was replaced with DMEM medium supplemented with 2% FBS (v/v) containing the treatments. Cell viability was evaluated at 24-, 48-, and 72-h intervals postincubation in a humidified atmosphere at 37 °C with 5% CO_2. To determine the viability percentage, the microplates were centrifuged at 250g for 10 min and 50 μL of the supernatants were transferred to new 96-well plates with 50 μL of LDH reagent. After a 30 min reaction, the stop solution was added. Absorbance was measured at 450 nm in a microplate reader (Multiskan FC Microplate Photometer, Thermo Fisher Scientific, MA). The percentage of viability was determined according to eq 4. A_S, A_{C-}, A_{C+} are the absorbances of the sample, negative control and positive control, respectively.

$$\text{cell viability (\%)} = \frac{A_S - A_{C-}}{A_{C+} - A_{C-}} \times 100 \quad (4)$$

2.5. Effect of Nanobioconjugates in A-375 and HaCaT Spheroids Analysis. Spheroids were formed in 96-well microplates with an ultralow attachment surface (Cat. #4520, Corning, Corning, NY). Briefly, 100 μL of DMEM supplemented with 10% (v/v) FBS at seeding densities of 8.75×10^5 cells/mL for HaCaT keratinocytes and 5×10^5 cells/mL for A-375 melanoma cells were added to each well. The microplate was centrifuged at 200g for 5 min and then placed on a rocking platform (Rocker 35 EZ, Vantaa, Southern Finland) at 120 rpm for 10 min. The cells were incubated in a humidified atmosphere at 37 °C and 5% CO_2. The next day, the formed spheroids were exposed to the nanoparticles by adding 100 μL of a 25 μg/mL solution of MNPs, MNPs−Si−PEGac−AEDP(TMZ), or MNPs−Si−PEGaa(PTX) to each well. For the control group, no nanoparticles were added. After 72 h of exposure to nanoparticles, the spheroids' viability was validated by incubating with Calcein AM (2 μM) and ethidium homodimer (4 μM) for 4 h. Fluorescent images were captured with an Olympus FV1000 confocal laser scanning microscope (CLSM) (Olympus, Japan) with excitation at 488 and 546 nm

https://doi.org/10.1021/acsomega.4c07415
ACS Omega 2024, 9, 45402−45420

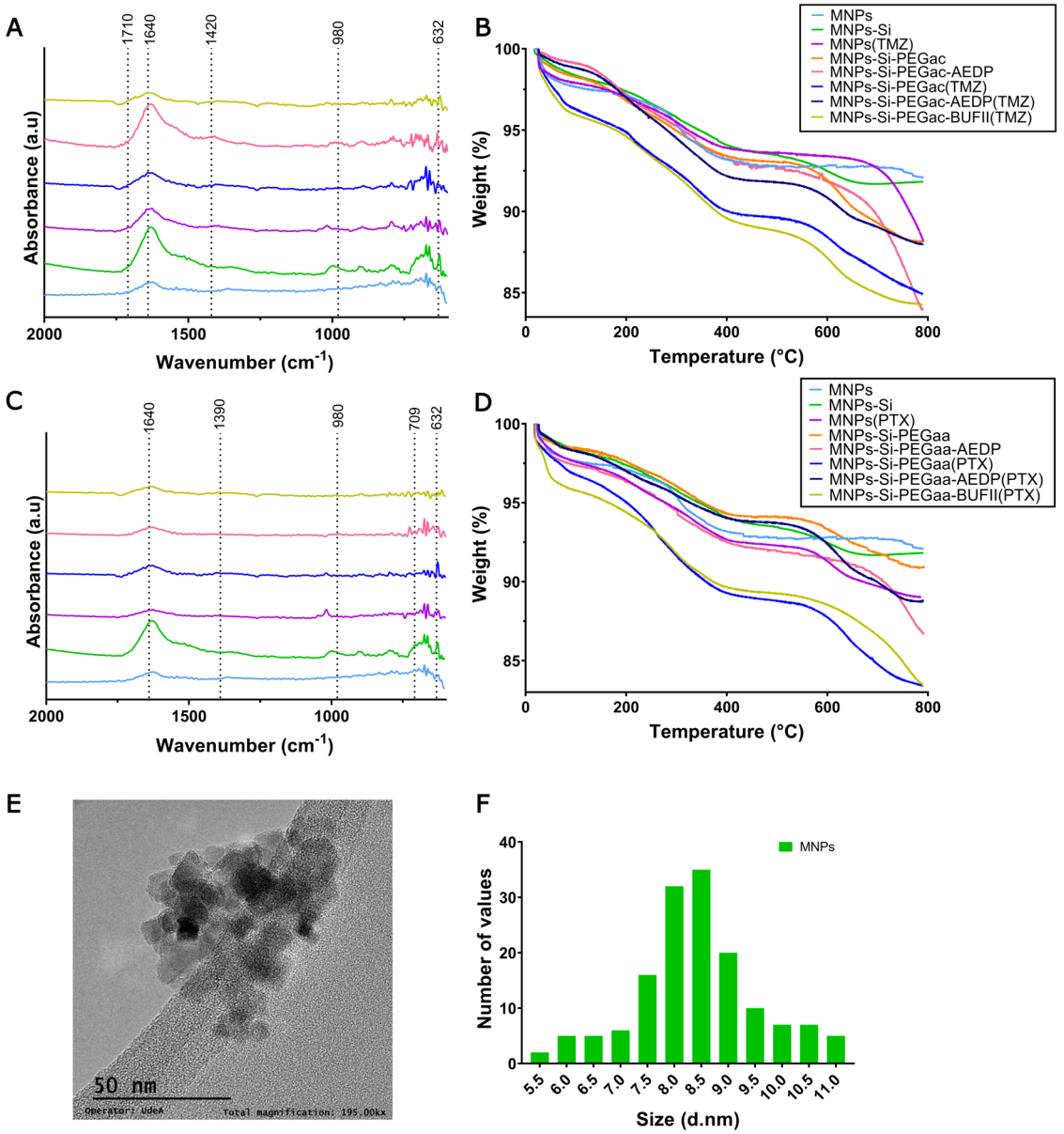

Figure 2. Physicochemical and microscopic characterization of nanobioconjugates. (A) FTIR spectra and (B) TGA analyses of TMZ nanoconjugates. (C) FTIR spectra and (D) TGA analyses of PTX nanoconjugates. (E) Microscopic characterization of bare MNPs. The morphology and size were analyzed through TEM at 145 kX. (F) Size distribution histogram of bare MNPs (based on TEM images).

lasers and emitted fluorescence capture at 517 and 617 nm, respectively. Transverse images were taken at 2 μm intervals (Z axis) with a 10X/0.30 UPlan FL N objective. Additionally, spheroids images were taken with a Zeiss Primovert Inverted Microscope (Zeiss, Germany) with a 4X/0.10 objective. Spheroids' morphology was analyzed by calculating the area, perimeter, and circularity using the MorphoLibJ 1.6.0.1 library in Fiji-ImageJ.

2.6. Cellular Internalization Pathways and Endosomal Escape Analysis. The cellular uptake and endosomal escape of the nanobioconjugates were determined via confocal microscopy for HaCaT keratinocytes and A-375 human melanoma cells. Cellular uptake was measured at 30 min and 4 h to capture both early and later stages of internalization. The 30 min time point was selected to observe initial uptake, providing insights into rapid internalization dynamics. The 4-h time point allowed for the assessment of subsequent internalization and potential endosomal escape.

Briefly, cells were resuspended in DMEM medium supplemented with 10% (v/v) FBS. 100 μL of a stock solution with a density of 2 × 10^5 cells/mL for HaCaT keratinocytes and 4 × 10^5 cells/mL for A-375 melanoma cells was added to a glass slide pretreated with poly-D lysine. After a 24-h incubation period to allow attachment, the medium was replaced with route inhibitors. Rottlerin, Filipin III, and Dynasore hydrate were used for macropinocytosis,[48,49] caveolae-mediated inhibition,[50] and clathrin-mediated inhibition,[48,51] respectively. The inhibitors were resuspended in nonsupplemented DMEM medium at concentrations of 6 μM for Rottlerin, 8 μg/mL for Filipin III, and 100 μM for Dynasore. Five evaluations were performed: inhibition of each endocytic-route, inhibition of the three endocytic-routes and a control without inhibitors. For the first four experiments, 250

https://doi.org/10.1021/acsomega.4c07415
ACS Omega 2024, 9, 45402−45420

μL of each inhibitor (or the three inhibitors) was added to the glass slide and incubated under a humidified atmosphere at 37 °C and 5% CO_2. Filipin III and Dynasore inhibitors were added 30 min after nanobioconjugates exposure, Rottlerin and the three inhibitors mixture were added 1 h before. After inhibition, cells were exposed to 250 μL (or 500 μL for the control) of Rhodamine B- or Propidium iodide-labeled nanobioconjugates in nonsupplemented DMEM medium at 25 μg/mL for 30 min and 4 h. Cells were washed with PBS 1X and exposed to nonsupplemented culture medium containing Hoechst 33342 (1:10000) and Lysotracker green DND-26 (1:10000) for 5 min. Images were captured using an Olympus FV1000 confocal laser scanning microscope (CLSM) (Olympus, Japan) with a 20X/0.75 UPlanSApo and a 40X/0.6 UCPlan FL N objective. Excitation/Emission wavelengths of 358 nm/461 nm, 488 nm/520 nm, and 546 nm/575 nm (for Rhodamine B-labeled nanoparticles) or 493 nm/636 nm (for Propidium iodide-labeled nanoparticles) were used for the detection of nuclei, endosomes, and nanobioconjugates, respectively. The analysis involved taking 10 images for each treatment (10 cells were segmented per image). Finally, image analysis was performed in Fiji-ImageJ to calculate colocalization and the percentage of area covered by the nanobioconjugates.

2.7. Statistical Analysis. All data measurements are reported as mean ± standard deviation. Each experiment was carried out in triplicate. Data analysis was performed using GraphPad Prism 8.0.1 software (San Diego, CA). Statistical comparisons were made employing a two-way ANOVA followed by either Sidak's or Dunnett's multiple comparisons test. Results with a p-value $\leq$ 0.05 (*) were considered statistically significant. The symbol * corresponds to statistically significant difference with a p-value in the range of 0.01 $\leq$ p-value $\leq$0.05, ** to statistically significant difference with a p-value in the range of 0.001 $\leq$ p-value <0.01, *** to p-value in the range of 0.0001 $\leq$ p-value $\leq$0.001, and **** to p-value <0.0001.

3. RESULTS

3.1. Synthesis, Functionalization, and Physicochemical Characterization of the Nanobioconjugates. Physicochemical characterizations of the TMZ and PTX nanobioconjugates are shown in Figure 2. Fourier Transform Infrared (FTIR) spectroscopy measurements were performed to confirm the correct immobilization of various compounds and drug loading on the nanobioconjugates' surfaces. The spectra from Figure 2A,C exhibit common peaks at 632 and 980 cm^{-1}, attributed to the Fe−O bonds of iron oxide[43] and the bond Si−O bonds, respectively, confirming silanization with APTES.[52,53] Another peak at 1640 cm^{-1} corresponds to amide I, confirming the successful immobilization of BUF-II and the PEG molecules on the nanobioconjugates.[43,52,53] The spectrum of the TMZ nanobioconjugates shows characteristic vibrational modes of the drug molecule, with a band at 1710 cm^{-1} attributed to the carbonyl groups (C=O) stretching,[54] and a band at 1420 cm^{-1} for C−N bending absorptions.[55] The PTX nanobioconjugates exhibit peaks at 709 cm^{-1} associated with C−H out-of-plane vibrations[56] and at 1390 cm^{-1} linked to the drug molecule's CH_3 vibrational modes.[56,57] These results collectively confirm the presence of conjugated molecules and drug loading on the surface of the nanobioconjugates.

Thermogravimetric Analysis (TGA) were conducted to assess the completeness of the synthesis steps, the conjugation efficiencies of the immobilized molecules, drug loading content, and the thermal stability of the nanobioconjugates. The thermograms obtained (Figure 2B,D) align well with those from previous studies, showing three main weight loss stages.[43,46,53,58,59] The first weight loss, between 65 and 200 °C, is associated with the loss of physically adsorbed water on the surface of the nanobioconjugates (sample dehydration). The second weight loss, from 200 to 400 °C, is attributed to residual organic and inorganic compounds adsorbed on the NPs surface (immobilization and synthesis reagents and impurities). The third weight loss, occurring above 400 °C, is associated with the detachment of APTES, PEGac or PEGac, AEDP, TMZ or PTX, and BUF-II.[43−45,58] Table 1 summarizes

Table 1. TGA Weight Loss Percentage for the Nanobioconjugates

	weight loss (%)	
nanobioconjugate	200−400 °C	above 400 °C
MNPs	3.9	
MNPs−Si	3.3	2.2
MNPs(TMZ)	3.9	5.2
MNPs(PTX)	3.8	5.8
MNPs−Si−PEGac	3.4	3.2
MNPs−Si−PEGac(TMZ)	4.8	5.1
MNPs−Si−PEGaa	3.3	3.3
MNPs−Si−PEGaa(PTX)	5.7	5.8
MNPs−Si−PEGac−AEDP	3.1	4.1
MNPs−Si−PEGac−AEDP(TMZ)	4.8	5.7
MNPs−Si−PEGaa−AEDP	3.7	3.6
MNPs−Si−PEGaa−AEDP(PTX)	2.9	5.2
MNPs−Si−PEGac−BUF-II(TMZ)	5.0	5.3
MNPs−Si−PEGaa−BUF-II(PTX)	4.7	6.2

the weight loss percentage from 200 to 400 °C and above 400 °C for the final nanobioconjugates and intermediate synthesis conjugates. According to the results, the drug loading content of the MNPs ranged from 1.6 to 3.6% (w/w) for TMZ and from 1.6 to 3.0% (w/w) for PTX, these values correspond to a drug loading efficiency of 32 to 72% for TMZ and 32% to 60% for PTX.

Nanoparticle size is a critical factor influencing the efficacy of nanoparticle-based drug delivery systems in biomedical applications, affecting biodistribution, cellular uptake, tissue penetration, toxicity, targeting ability, and drug or therapeutic molecule half-life.[4,60,61] The size of nanobioconjugates was analyzed individually using Transmission Electron Microscopy (TEM) imaging, while their hydrodynamic diameter was determined by Dynamic Light Scattering (DLS) measurements.

TEM images for bare MNPs (Figure 2E) and nanobioconjugates (Supplemental Figure S2) show that the majority of MNPs appear as clusters. This aggregation is likely due to the magnetostatic interactions between magnetite particles.[62] The largest observed aggregates were approximately 200 nm in size. The average diameter of bare MNPs was 8.4 ± 1.1 nm for, whereas the average diameters for TMZ and PTX nanobioconjugates were larger, measuring 13.0 ± 2.3 and 14.4 ± 1.9 nm, respectively. The irregular shape of the aggregates may be attributed to the synthesis method, the choice of alkaline solution, and other factors such as pH and

https://doi.org/10.1021/acsomega.4c07415
ACS Omega 2024, 9, 45402−45420

Table 2. Nanoparticles Size, Polydispersity Index and Zeta Potential for the Nanobioconjugates

nanobioconjugate	average diameter (nm)	polydispersity index	zeta potential (mV)	
			pH 5.5	pH 7.0
MNPs	99.47 ± 2.71	0.177 ± 0.005	19.6 ± 0.4	−14.1 ± 0.6
MNPs(TMZ)	102.9 ± 2.18	0.172 ± 0.014	22.3 ± 0.7	−21.7 ± 0.5
MNPs(PTX)	103.2 ± 2.08	0.186 ± 0.011	20.9 ± 0.7	−15.8 ± 0.6
MNPs−Si−PEGac(TMZ)	112.4 ± 2.72	0.109 ± 0.013	23.4 ± 0.4	−26.5 ± 0.2
MNPs−Si−PEGaa(PTX)	115.9 ± 2.29	0.160 ± 0.059	25.1 ± 0.4	−28.2 ± 0.1
MNPs−Si−PEGac−BUF-II(TMZ)	126.7 ± 2.19	0.110 ± 0.013	16.4 ± 0.2	−22.9 ± 0.4
MNPs−Si−PEGaa−BUF-II(PTX)	127.3 ± 2.93	0.152 ± 0.009	18.1 ± 0.4	−24.3 ± 0.4
MNPs−Si−PEGac−AEDP(TMZ)	125.2 ± 2.34	0.170 ± 0.010	26.1 ± 0.5	−29.6 ± 0.1
MNPs−Si−PEGaa−AEDP(PTX)	130.6 ± 2.10	0.106 ± 0.012	24.2 ± 0.6	−27.1 ± 0.3

the rate of alkaline solution addition during the process.[63] The observed increase in aggregate size with the immobilization of molecules and drug loading can be attributed to a reduction in repulsive forces between nanoparticles and enhanced hydrophobic interactions, resulting in the formation of larger clusters.[58]

Table 2 compiles the average hydrodynamic diameter, Polydispersity Index (PDI), and zeta potential for the nanobioconjugates. The nanobioconjugates presented an average hydrodynamic diameter ranging from 99.47 ± 2.71 to 130.6 ± 2.10 nm. As observed in TEM images, the nanoparticles tended to aggregate in solution. However, according to Y. Yao et al.[5] and L. Meylina et al.,[64] the optimal particle size for cancer treatment typically falls within the range of 10−200 nm, facilitating effective penetration of leaky tumor blood vessels and accumulation in tumor tissue through the EPR effect. The size difference between the bare MNPs and the nanobioconjugates is attributed to the conducted functionalizations (silanization with APTES and immobilization of PEGaa, PEGac, AEDP, and BUF-II). All synthesized nanobioconjugates had a PDI below 0.2, which is optimal and consistent with findings reported in other studies.[45,65]

The zeta potential characterizes the electrokinetic potential of colloidal systems and quantifies their surface charge.[66] Zeta potential assessment was used to evaluate suspension stability, surface charge under biological pH conditions, and potential cellular uptake pathways for the nanobioconjugates. Bare MNPs exhibited a zeta potential of 19.6 ± 0.4 at the lower pH of 5.5, characteristic of the acidic environment found in endosomes and lysosomes. This shifted to −14.1 ± 0.6 mV at the neutral pH of 7.0, which reflects the conditions found in blood and the cytoplasm. The nanobioconjugates displayed zeta potential values ranging from 16.4 ± 0.2 to 26.1 ± 0.5 mV at pH 5.5, and from −14.1 ± 0.6 to −29.6 ± 0.1 mV at pH 7.0, consistent with previous findings.[67,68] The isoelectric point (pI) of the MNPs was calculated to be around pH 6.4. At pH 5.5, which is below the pI, functional groups on the MNP surface, such as amine, hydroxyl, and carboxyl groups, become protonated, resulting in a more positive surface charge. Conversely, at pH 7.0, which is above the pI, these groups deprotonate, leading to a more negative surface charge. This explains the observed shift in nanoparticle behavior.[69,70] High zeta potential values, either above +25 mV or below −25 mV, are associated with nanoparticles that are stable in suspension without tendencies for coagulation or flocculation.[71]

It has been proved that nanoparticles with a stronger charge exhibit better colloidal stability due to repulsion between particles.[66] Moreover, the obtained zeta potential values are in line with those from other studies where nanoparticles were modified with anticancer drugs such as TMZ and PTX, and PEG.[72−74] These results suggest that the primary entry routes for these nanobioconjugates into cells are through endocytic pathways, particularly via macropinocytosis, clathrin-mediated endocytosis, and caveolin-mediated endocytosis.[75]

The magnetic response of nanobioconjugates synthesized at different time intervals (see Supplemental Figure S1) was evaluated to determine the persistence of their magnetic properties over time. The results show that the magnetic response remained consistent throughout the year following synthesis, with only a slight decrease in the magnetic response of a small fraction of nanoparticles, reinforcing their potential to be magnetically controlled by an external field to enhance tumor targeting.

3.2. Biocompatibility Studies. Figure 3 illustrates the hemolytic activity and platelet aggregation effects of the nanobioconjugates, as well as cell viability in HaCaT keratinocytes and A-375 human melanoma cells 72 h postexposure to the nanobioconjugates at a concentration of 25 μg/mL. This concentration was selected to compare the effectiveness of the nanobioconjugates because, at this concentration, bare MNPs maintain cell viability above 80%, having been established previously as a noncytotoxic concentration for the bare nanocarrier.[58] This allows for a comparison based on the action of the drug-loaded nanobioconjugates rather than the cytotoxicity associated with the bare MNPs.

All treatments exhibited an average hemolytic activity below 1%, and no significant platelet aggregation was observed compared to the negative control. According to ISO standard 10993-4:2018, these results highlight the nanobioconjugates' high hemocompatibility, suggesting their suitability for intravenous administration and low risk of causing thrombosis. Cytotoxicity results revealed that MNPs−Si−PEGac−AEDP(TMZ) and MNPs−Si−PEGaa(PTX) nanobioconjugates exhibited higher cytotoxicity in cancer cells relative to healthy cells and outperformed free drugs.

Notably, the free drugs were evaluated at concentrations four times higher than those in the nanobioconjugates. Despite this, MNPs−Si−PEGac−AEDP(TMZ) and MNPs−Si−PEGaa(PTX) nanobioconjugates showed superior performance against A-375 human melanoma cells, suggesting that the nanobioconjugates effectively improved the low water solubility of these drugs.

Additionally, Supplemental Figures S3−S6 show the cytotoxicity results at 24-, 48-, and 72 h postexposure to the TMZ and PTX nanobioconjugates, as well as the effect of the free drugs at different concentrations on HaCaT keratinocytes and A-375 human melanoma cells. The nanobioconjugates

https://doi.org/10.1021/acsomega.4c07415
ACS Omega 2024, 9, 45402−45420

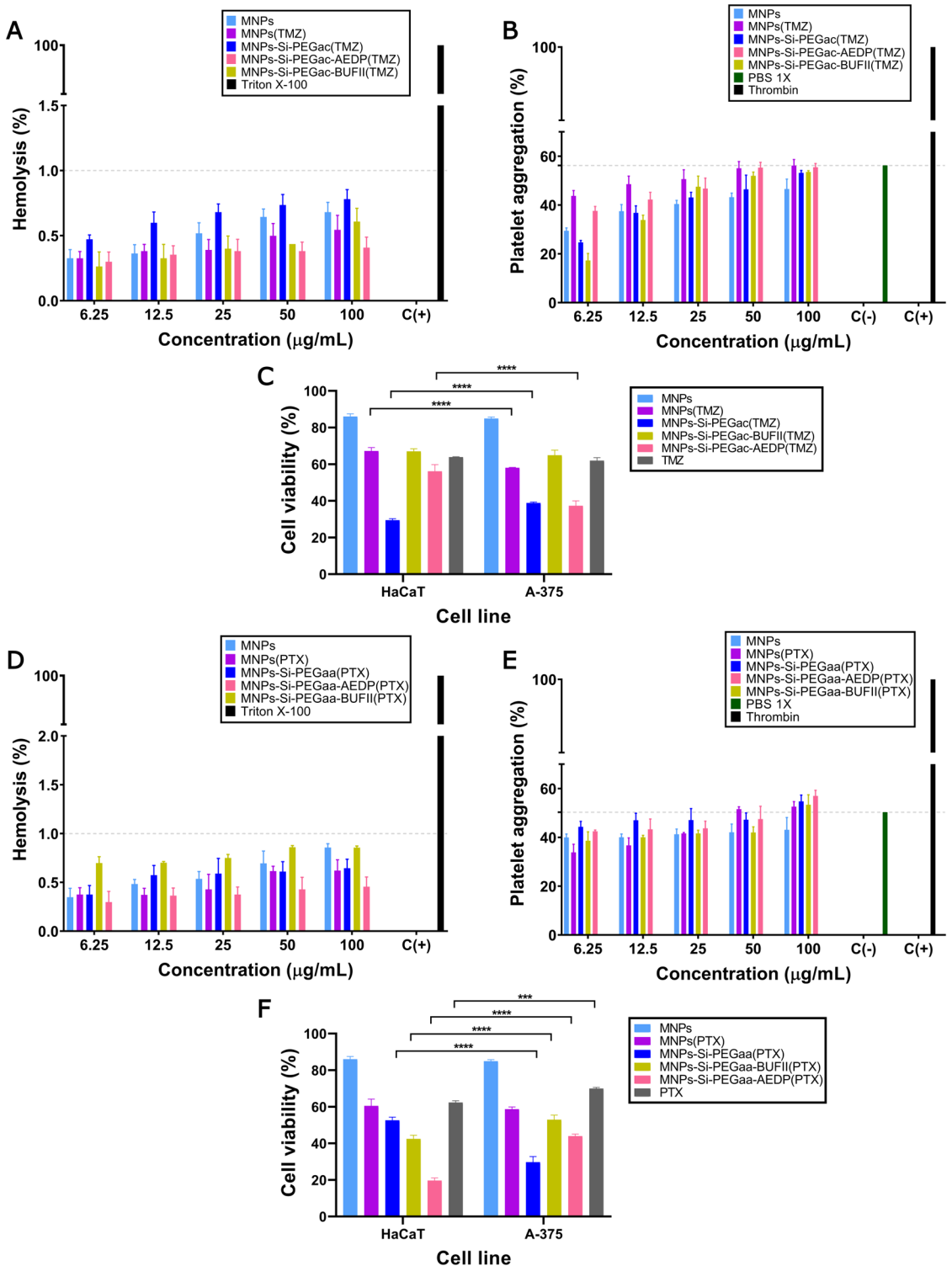

Figure 3. Biocompatibility assays of the nanobioconjugates. (A) Hemolytic effect, (B) platelet aggregation and, (C) cytotoxicity of the TMZ nanobioconjugates. (D) Hemolytic effect, (E) platelet aggregation and, (F) cytotoxicity of the PTX nanobioconjugates. Cell viability is represented for the nanobioconjugates evaluated at 25 μg/mL at 72 h. The symbol * corresponds to a statistically significant difference with a p-value in the range of $0.01 \leq p$-value ≤ 0.05, ** to a statistically significant difference with a p-value in the range of $0.001 \leq p$-value < 0.01, *** to p-value in the range of $0.0001 \leq p$-value ≤ 0.001 and **** to p-value < 0.0001.

exhibited a significantly higher cytotoxic effect compared to the bare MNPs. The greatest effectiveness of the nanobioconjugates was observed at 72 h postexposure where the nanobioconjugates resulted in increased cytotoxicity compared to the free drugs at their corresponding concentrations.

3.3. Effect of Nanobioconjugates in A-375 and HaCaT Spheroids. Spheroids were employed as a basic model to mimic the physical interactions of cells in tumor tissues *in vitro*. To understand the impact of TMZ and PTX nanobioconjugates on HaCaT keratinocytes and A-375 human

https://doi.org/10.1021/acsomega.4c07415
ACS Omega 2024, 9, 45402−45420

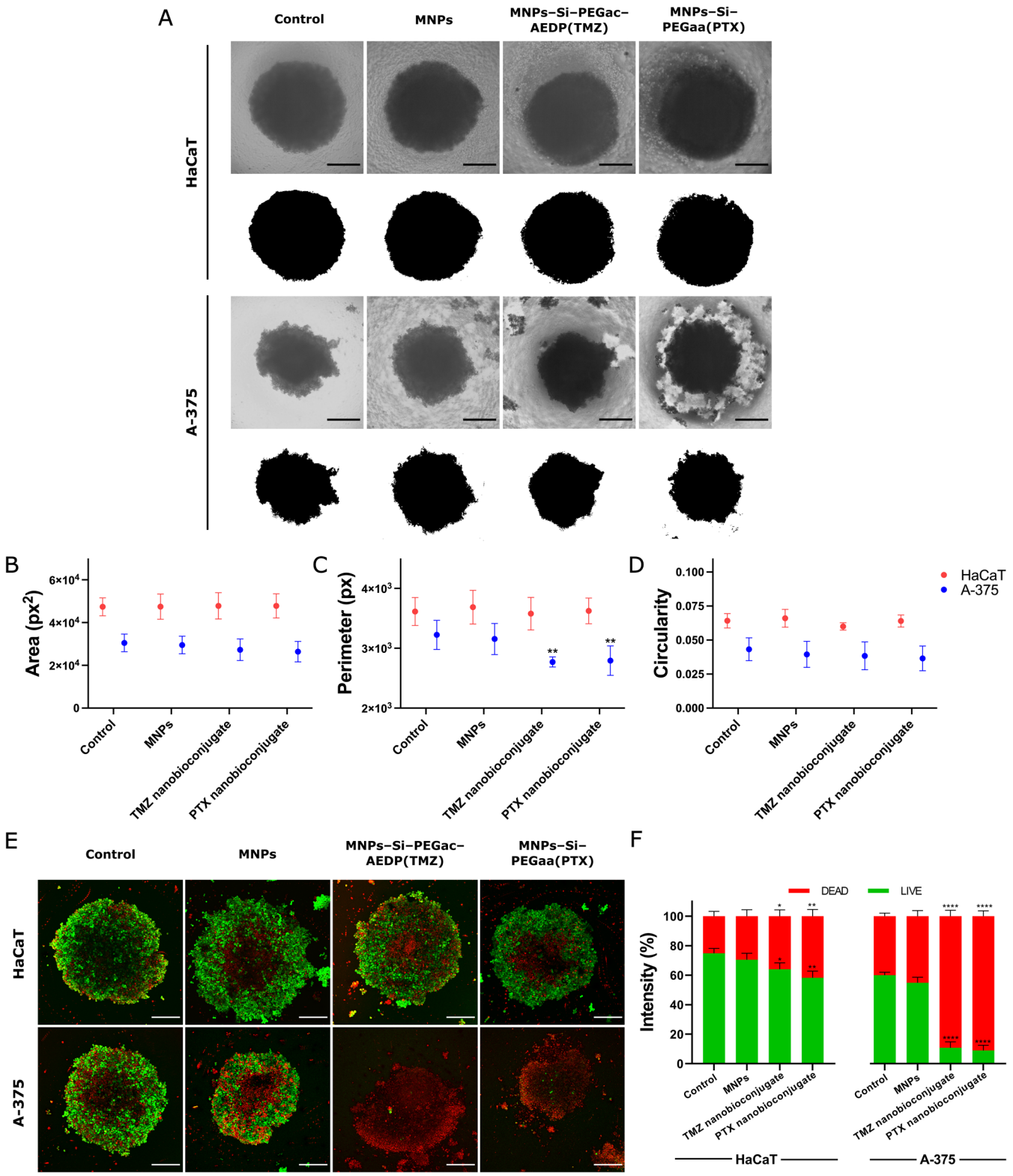

Figure 4. A-375 and HaCaT spheroids morphology and cell viability after 72 h of exposure to bare MNPs, TMZ nanobioconjugate, and PTX nanobioconjugate evaluated at 25 μg/mL and the control without nanoparticles. (A) Images were obtained by using a 4X objective, below each image, the mask used for the analysis of the morphology is shown. The scale bar corresponds to 500 μm (B) area, (C) perimeter, and (D) circularity graphics. (E) Confocal images were obtained by using 10X objective. Calcein AM was used to label LIVE cells and Ethidium Homodimer was used to label DEAD cells. Scale bar corresponds to 250 μm. (F) Fluorescence intensity for green and red channels. The symbol * corresponds to a statistically significant difference with a p-value in the range of $0.01 \leq p\text{-value} \leq 0.05$, ** to a statistically significant difference with a p-value in the range of $0.001 \leq p\text{-value} < 0.01$, *** to p-value in the range of $0.0001 \leq p\text{-value} \leq 0.001$ and **** to p-value < 0.0001.

https://doi.org/10.1021/acsomega.4c07415
ACS Omega 2024, 9, 45402−45420

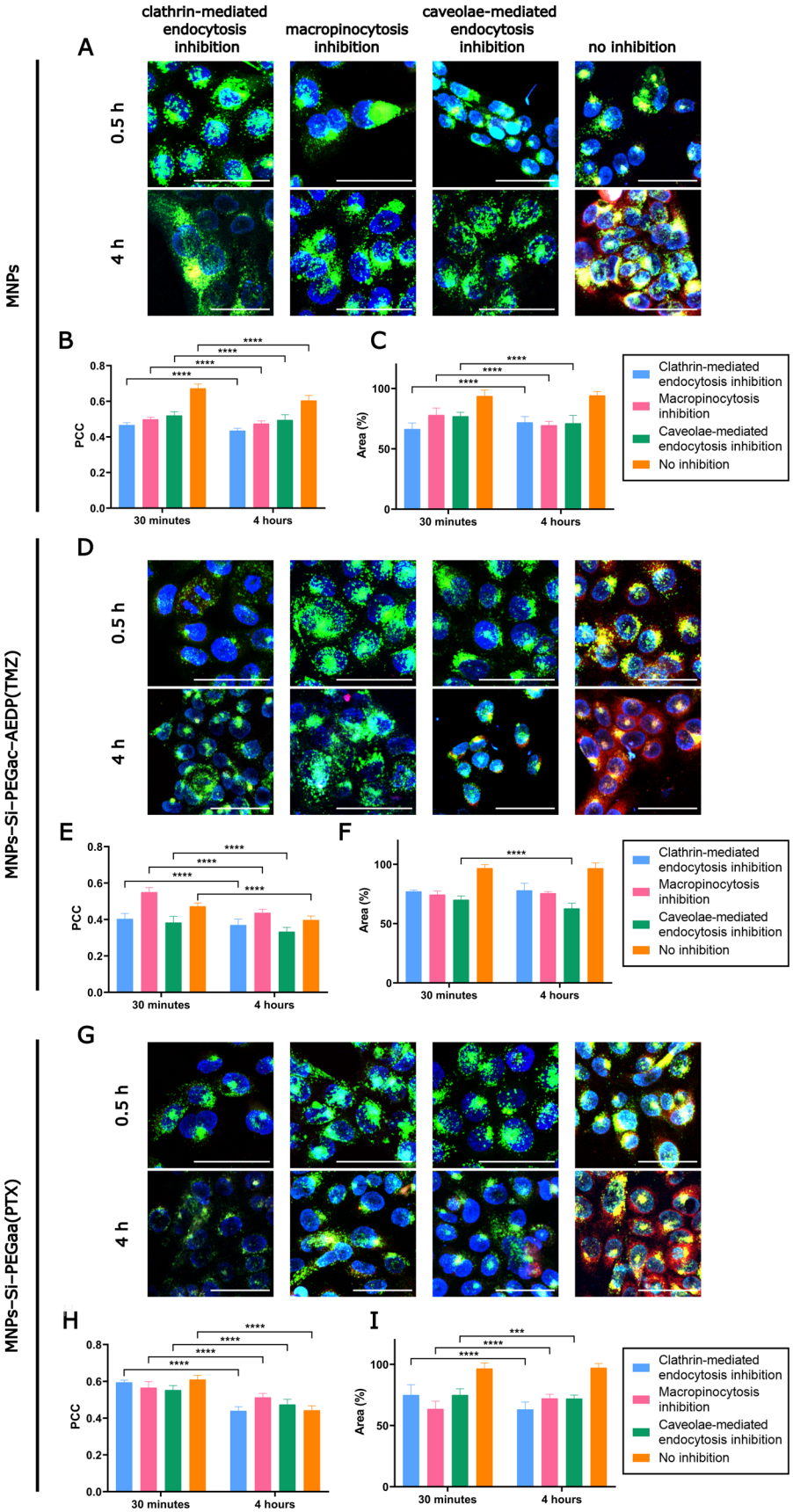

Figure 5. Confocal microscopy images for cell-internalization pathways and endosomal escape analysis, Pearson Correlation Coefficient (PCC) and percentage of intracellular area covered by Rhodamine-B labeled MNPs, Propidium Iodide labeled MNPs−Si−PEGac−AEDP(TMZ) and Rhodamine-B labeled MNPs−Si−PEGaa(PTX) in HaCaT cells at 0.5 and 4 h after the nanobioconjugates exposure. The scale bars correspond to 50 μm. In (A), (D), and (G) the images show the nuclei labeled with Hoechst (blue), endosomes with Lysotracker Green (green), and

https://doi.org/10.1021/acsomega.4c07415
ACS Omega 2024, 9, 45402−45420

Figure 5. continued

nanobioconjugates with Rhodamine-B or Propidium iodide (red). The yellow areas correspond to colocalization between red and green channels, indicating lysosomal entrapment. (B), (E), and (H) correspond to the PCC of the nanobioconjugates in HaCaT cells. Higher PCC values denote a greater correlation between the red and green channels, indicating lysosomal entrapment. (C), (F), and (I) show the covered area percentage for the nanobioconjugates in HaCaT cells. The symbol * corresponds to a statistically significant difference with a p-value in the range of $0.01 \leq p$-value ≤ 0.05, ** to a statistically significant difference with a p-value in the range of $0.001 \leq p$-value < 0.01, *** to p-value in the range of $0.0001 \leq p$-value ≤ 0.001 and **** to p-value < 0.0001.

melanoma cell spheroids, two evaluations were conducted, as presented in Figure 4. Nanobioconjugates that exhibited the highest selectivity for A-375 human melanoma cells in the previous cytotoxicity assay, specifically MNPs−Si−PEGac−AEDP(TMZ) and MNPs−Si−PEGaa(PTX), were evaluated against bare MNPs.

Initially, we examined morphological attributes such as area, perimeter, and circularity to assess the effect of the treatments. Figure 4A provides visual representations, highlighting typical outlines for both HaCaT and A-375 spheroids. For HaCaT spheroids, there was no noticeable difference in these attributes compared to the untreated samples (Figure 4B−D). However, A-375 spheroids exhibited significant changes in perimeter and circularity when treated with TMZ and PTX nanobioconjugates, compared to untreated spheroids or those exposed to bare MNPs. The observed decrease in area, perimeter, and circularity suggests that cells on the surface of A-375 spheroids may be detaching when exposed to the nanobioconjugates.

The viability of the spheroids was further confirmed via LIVE/DEAD staining (Figure 4E,F). The TMZ and PTX nanobioconjugates had minimal impact on the viability of HaCaT spheroids but significantly affected the A-375 spheroids. Compared to the control group, it was evident that A-375 spheroids were inherently more sensitive than HaCaT spheroids. This suggests that the observed outcome may result from a combination of the nanobioconjugates' effect and the inherent sensitivity of the A-375 spheroids.

3.4. Cellular Internalization Pathways and Endosomal Escape Analysis. Confocal microscopy was used to study the internalization mechanisms of the bare MNPs and MNPs−Si−PEGac−AEDP(TMZ) and MNPs−Si−PEGaa-(PTX) selected nanobioconjugates. To discern the uptake mechanisms of the nanobioconjugates, Rottlerin, Filipin III and Dynasore inhibitors were used. Particularly, Rottlerin inhibits the activity of protein kinase C delta and can affect most endocytic mechanisms;[76] however, is usually used for analyzing macropinocytosis uptake.[48,49] Filipin III, on the other hand, interacts with cholesterol at the cell membrane and is used to inhibit caveolin-mediated endocytosis.[50] Finally, Dynasore, inhibits the GTPase activity of dynamin1, dynamin2 and Drp1, the mitochondrial dynamin, and may interfere with cholesterol homeostasis and actin.[51] It is frequently used for inducing clathrin-mediated inhibition.[48]

Figures 5 and 6 present confocal images and results regarding the internalization routes and endosomal escape analysis for HaCaT keratinocytes and A-375 human melanoma cells (detailed images are available in the Supporting Information, Supplemental Figures S7, S8, S9, S10, S11, S12). The accompanying graphics summarize the percentages of covered area by the bare MNPs and the nanobioconjugates, as well as the Pearson Correlation Coefficient (PCC) values associated with the colocalization of the bare MNPs and the nanobioconjugates with lysosomes in both cell lines.

For the TMZ nanobioconjugate (MNPs−Si−PEGac−AEDP(TMZ)), the percentage of endosomal escape in HaCaT keratinocytes ranged from 8.34 to 20.6%, while in A-375 human melanoma cells, it ranged from 19.7 to 27.6%. For the PTX nanobioconjugate (MNPs−Si−PEGaa(PTX)), the percentage of endosomal escape in HaCaT keratinocytes ranged from 9.35 to 27.5%, and in A-375 human melanoma cells, it ranged from 11.0 to 33.5%. These results indicate that the nanobioconjugates achieved a higher endosomal escape percentage in melanoma cells compared to the keratinocytes. In contrast, the bare MNPs showed endosomal escape percentages between 4.83 and 10.1% in HaCaT keratinocytes, and between 5.58 and 9.29% in A-375 human melanoma cells. As reported in previous works, the functionalization of nanoparticles generally improved their endosomal escape capabilities.[45,46,59]

The percentages of the covered area by the nanobioconjugates without endocytic inhibition were above 96% for TMZ and PTX nanobioconjugates and nearly 94% for bare MNPs in both cell lines, affirming their potential as drug delivery systems. For the TMZ nanobioconjugate, the covered area percentages ranged from 62 to 78% for HaCaT keratinocytes and from 62 to 75% for A-375 human melanoma cells. For the PTX nanobioconjugate, the covered area percentages ranged from 63 to 74% for HaCaT keratinocytes and from 59 to 76% for A-375 melanoma cells. These results were used to calculate the endocytic-mediated internalization in HaCaT keratinocytes and A-375 human melanoma cells at 30 min and 4 h postexposure to the nanobioconjugates, summarized in Table 3.

The main findings suggest that the endocytosis of the TMZ nanobioconjugate was primarily mediated by caveolae-mediated endocytosis in both cell lines. In contrast, the PTX nanobioconjugate's endocytosis was primarily mediated by macropinocytosis in HaCaT keratinocytes and by caveolae-mediated endocytosis in A-375 human melanoma cells. Bare MNPs were primarily internalized into the cells through clathrin-mediated endocytosis in both cell lines. Further analysis is detailed in the Discussion section.

4. DISCUSSION

An ideal nanoparticle drug delivery system should be able to reach, bind, and deliver its load to specific pathological tissues while minimizing or avoiding drug-induced damage to healthy tissues. Size, shape, surface charge, thermal stability, toxicity, binding capacity, and drug loading efficiency are essential for successful drug delivery. In our study, we developed MNPs using the chemical coprecipitation method, which were found to possess suitable characteristics for the delivery of PTX and TMZ to human melanoma cells.

In general, the MNPs exhibited a morphology consistent with previous works.[44,45,58] The nanobioconjugates have an average hydrodynamic diameter under 150 nm, which is optimal for penetrating leaky tumor blood vessels and

https://doi.org/10.1021/acsomega.4c07415
ACS Omega 2024, 9, 45402−45420

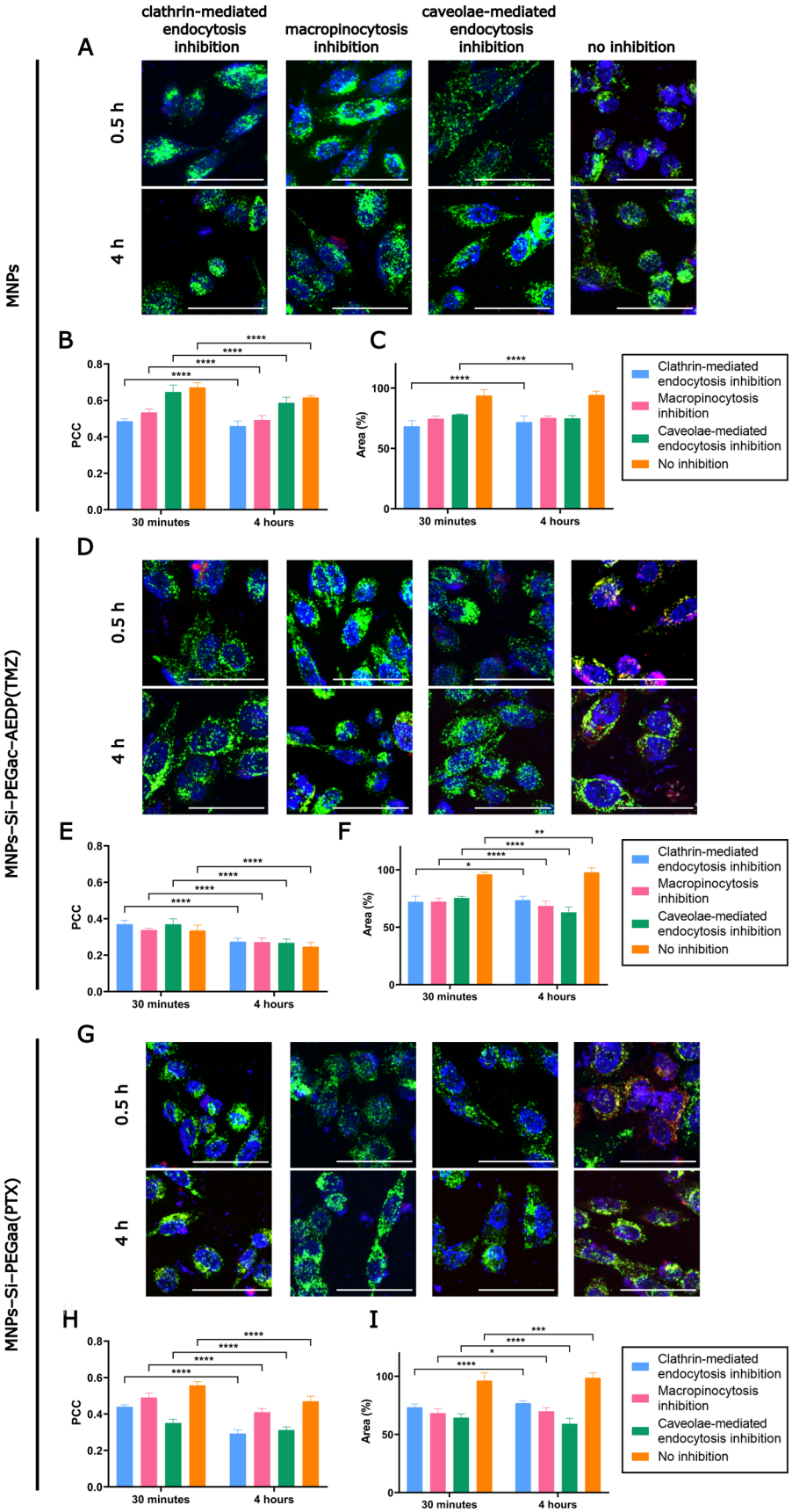

Figure 6. Confocal microscopy images for cell-internalization pathways and endosomal escape analysis, Pearson Correlation Coefficient (PCC) and percentage of intracellular area covered by Rhodamine-B labeled MNPs, Propidium Iodide labeled MNPs−Si−PEGac−AEDP(TMZ) and Rhodamine-B labeled MNPs−Si−PEGaa(PTX) in A-375 cells at 0.5 and 4 h after the nanobioconjugates exposure. The scale bars correspond to 50 μm. In (A), (D), and (G) the images show the nuclei labeled with Hoechst (blue), endosomes with Lysotracker Green (green), and

https://doi.org/10.1021/acsomega.4c07415
ACS Omega 2024, 9, 45402−45420

Figure 6. continued

nanobioconjugates with Rhodamine-B or Propidium iodide (red). The yellow areas correspond to colocalization between red and green channels, indicating lysosomal entrapment. (B), (E), and (H) correspond to the PCC of the nanobioconjugates in A-375 cells. Higher PCC values denote a greater correlation between the red and green channels, indicating lysosomal entrapment. (C), (F), and (I) show the covered area percentage for the nanobioconjugates in A-375 cells. The symbol * corresponds to a statistically significant difference with a p-value in the range of $0.01 \leq p$-value ≤ 0.05, ** to a statistically significant difference with a p-value in the range of $0.001 \leq p$-value < 0.01, *** to p-value in the range of $0.0001 \leq p$-value ≤ 0.001 and **** to p-value < 0.0001.

accumulating within tumor tissue.[5,64] This size range leverages the EPR effect, leading to reduced adverse effects. The nanobioconjugates' size suggests they could evade renal clearance and capture by the reticuloendothelial system (RES), making them suitable for intravenous administration. This characteristic could potentially offer prolonged circulation and enhanced bioavailability.[58]

TGA offers a rapid and efficient method for measuring drug loading and immobilization content in a single-step process.[47] The drug loading efficiency for the nanobioconjugates ranged between 32 and 72%. FTIR results confirmed the presence of the functional molecules PEG, AEDP, and BUF-II, as well as the drugs PTX and TMZ on the nanobioconjugates' surface. This was evidenced by their characteristic peaks, particularly the carbonyl groups (C═O) stretching[54] and C−N bending absorptions[55] bands of TMZ, and the bands associated with the C−H bond[56] and CH_3 vibrational modes of PTX.[56,57] Studies suggest that drug loading onto IONPs involves a combination of electrostatic interactions, hydrogen bonding, and van der Waals forces.[77−79] For instance, drug molecules primarily bind to functionalized nanoparticles through electrostatic interactions, where protonated chemical groups form strong bonds with negatively charged regions on the nanoparticle surface. These interactions are further stabilized by hydrogen bonds with surface molecules, such as PEG or AEDP. TMZ and PTX were likely loaded onto the nanoparticles through surface interactions, interactions with immobilized molecules, or via the nanoparticle's porosity.

Nanoparticle surface charge is an important consideration in targeting drug delivery.[80] Cell surfaces, particularly those of cancer cells, are typically negatively charged due to the translocation of negatively charged constituents from the inner layer of the cell membrane to the cell surface (e.g., phosphatidylserine, anionic phospholipids, glycoproteins, and proteoglycans).[81] Over the past five decades, evidence has shown that the pH of most solid tumors in patients ranges from 5.7 to 7.8, with over 80% of these values being below pH 7.2.[82] Tumor tissues exhibit large, acid-outside plasma pH gradients, whereas normal tissues generally have alkaline-outside pH gradients.[83] Consequently, the extracellular pH of malignant tumors is significantly lower than that of normal tissues under physiological conditions.[84] The nanobioconjugates demonstrated that as the pH became more acidic (lower than 6.4), the zeta potential shifted to a positive value. This behavior, observed in other studies, enhances the electrostatic interaction between the nanoparticles and tumor tissues, leading to tumor-specific accumulation.[80]

Previous reports have also confirmed that the surface charge reversal behavior of nanoparticles in the acidic environment of endolysosomes is crucial for their escape from these compartments.[85,86] The protonation of nanoparticles during luminal acidification induces the proton-sponge effect or other mechanisms that disrupt the endosome, facilitating the escape of nanoparticles into the cytoplasm.[75] Additionally, the superficial charge can influence cellular uptake mechanisms. In our case, the nanobioconjugates exhibited a strong negative charge, below −25 mV. The uptake of IONPs with higher anionic surface charges (−48 and −25 mV) is attributed to mechanisms mediated by macropinocytosis, clathrin-dependent, and caveolin-dependent pathways.[75]

The hemocompatibility of the nanobioconjugates, as per ISO standard 10993-4:2018, underscores their suitability for intravenous administration and low risk of causing thrombosis. Final nanobioconjugates were selected for their reduced cytotoxicity in HaCaT keratinocytes and high cytotoxicity in A-375 human melanoma cells. Considering these factors, MNPs−Si−PEGac−AEDP(TMZ) (TMZ nanobioconjugate) and MNPs−Si−PEGaa(PTX) (PTX nanobioconjugate) were chosen for further evaluation in spheroids and their cell internalization routes. Interestingly, neither of the final nanobioconjugates included the peptide BUF-II, despite initial hypotheses suggesting that this peptide could provide cancer-selective cytotoxicity.[41,42] Previous studies have indicated that the hybrid peptide Buforin IIb, derived from BUF-II, exhibits stronger cytolytic activity against cancer cells by specifically targeting them through interaction with cell surface gangliosides.[87−89] This potential will be explored in future research.

Moreover, the selected TMZ and PTX nanobioconjugates exhibited not only a high cytotoxic effect against 2D cultures of A-375 human melanoma cells but also demonstrated selective cytotoxicity against A-375 spheroids while sparing HaCaT spheroids. Drug release from the MNPs appears to be primarily governed by environmental changes, such as pH and ionic strength. Upon cellular entry, endosomal entrapment may alter ionic strength, triggering the desorption of the drug from the nanoparticle surface.[90,91]

The findings indicate that PEGylation improved drug loading and enhanced the effectiveness of the nanobioconjugates, consistent with previous studies.[92,93] Typically, PEGylation is employed to shield nanoparticles from aggregation, opsonization, and phagocytosis, thereby prolonging systemic circulation due to the polymer's presumed inert interaction with proteins.[94] However, PEG alone has been shown to interact with P-glycoprotein in intestinal cells and induce apoptosis in human colon cancer cells.[95−98] A recent study on A-375 metastatic melanoma cells found that PEG reduced cell viability, with this effect depending on PEG's molecular weight and concentration.[99] Nonetheless, it is important to note that PEG produced similar reductions in cell viability in murine 3T3 fibroblast and human corneal epithelial cell lines. This raises a concern to the authors that PEG not only enhanced drug loading but also contributed to the cytotoxic effect of the nanobioconjugates against A-375 cells, as observed with the most cytotoxic nanobioconjugate MNPs−Si−PEGaa(PTX).

One of the most important findings of this study is the confirmation of nanobioconjugates' general multipathway mechanism for cell internalization. The TMZ nanobioconjugate endocytosis in both cell lines and PTX nanobioconjugate

https://doi.org/10.1021/acsomega.4c07415
ACS Omega 2024, 9, 45402−45420

Table 3. Endocytic-Mediated Internalization in HaCaT Keratinocytes and A-375 Human Melanoma Cells at 30 min and 4 h Post-exposure to the Nanobioconjugates

		endocytic-mediated internalization (%)							
		clathrin-mediated endocytosis		macropinocytosis		caveolin-mediated endocytosis		other routes	
	nanobioconjugate	30 min	4 h	30 min	4 h	30 min	4 h	30 min	4 h
HaCaT	MNPs	33.6 ± 5.03	28.1 ± 4.85	22.0 ± 5.81	30.5 ± 3.20	23.0 ± 3.30	28.8 ± 4.50	21.3 ± 1.55	12.6 ± 3.23
	MNPs–Si–PEGac–AEDP(TMZ)	25.0 ± 8.42	36.8 ± 4.07	36.4 ± 6.30	27.9 ± 3.42	25.0 ± 5.00	28.0 ± 2.84	13.5 ± 4.08	7.33 ± 4.42
	MNPs–Si–PEGaa(PTX)	22.9 ± 1.19	21.9 ± 4.89	25.6 ± 3.03	24.4 ± 1.34	29.9 ± 3.24	37.2 ± 4.49	21.6 ± 1.52	16.5 ± 1.91
A-375	MNPs	31.7 ± 4.74	28.2 ± 4.20	25.4 ± 2.11	24.8 ± 1.77	22.0 ± 0.64	25.1 ± 2.33	20.8 ± 4.64	21.8 ± 3.33
	MNPs–Si–PEGac–AEDP(TMZ)	26.7 ± 2.93	23.2 ± 2.04	31.7 ± 3.90	30.1 ± 3.01	35.6 ± 3.32	40.9 ± 4.76	5.97 ± 2.32	5.75 ± 2.76
	MNPs–Si–PEGaa(PTX)	27.9 ± 4.90	26.4 ± 3.32	27.7 ± 3.00	31.5 ± 4.28	24.6 ± 1.43	37.0 ± 4.69	19.8 ± 4.01	5.07 ± 2.24

endocytosis in A-375 melanoma cells were primarily mediated by caveolae-mediated endocytosis. Endocytosis routes, such as caveolae-mediated and clathrin-mediated, are common for IONPs uptake.[75] PTX nanobioconjugate endocytosis was primarily mediated by macropinocytosis for HaCaT keratinocytes. The uptake of NPs by macropinocytosis proceeds by nonspecific interactions with the plasma membrane through ruffle formation.[100] As a result, uptake via this mechanism is usually not affected by NP properties such as size or shape. Nevertheless, it is possible that IONPs functionalized with specific molecules as PEG can stimulate macropinocytosis.[101,102] Bare MNPs were internalized into the cells primarily by clathrin-mediated endocytosis in both cell lines. Usually, nanoparticles internalized via clathrin-mediated endocytosis typically end up in lysosomes.[103] Consistent with this, the results showed that when this route was inhibited, MNPs exhibited the lowest PCC, indicating that this route is effectively associated with the endosomal entrapment of the MNPs.

Consistent with other reports, IONPs with negative zeta potential are mainly internalized by clathrin- and caveolae-dependent endocytosis and macropinocytosis.[101,102,104−107] Although the exact mechanisms governing the endocytosis of anionic nanoparticles (ANPs) are not entirely clear, several studies suggest that their uptake involves inducing local changes in membrane properties.[75] Wang et al. explained that ANP interactions with the plasma membrane are more likely in phosphatidylcholine-rich domains due to their headgroup's electric dipole of phosphate and choline (P^--N^+).[108] Consequently, ANPs can preferentially interact with the N+ terminus of phosphatidylcholine molecules, causing a slight tilt in their membrane position, leading to local membrane gelation. This ANP-induced membrane budding can trigger endocytic processes, allowing all endocytic routes to contribute to the internalization of anionic-coated IONPs.[75]

Previous studies have demonstrated that IONPs are typically metabolized in the liver and other organs of the mononuclear phagocytic system (MPS). These nanoparticles are broken down into various ferrous (Fe^{2+}) and ferric (Fe^{3+}) products. Once degraded, these iron products are recycled and eventually incorporated into the body's natural iron storage or utilization pathways (e.g., hemoglobin, ferritin, and transferrin).[109,110] This recycling process underscores the biocompatibility and potential therapeutic utility of IONPs in drug delivery applications.

Magnetic nanoparticles have demonstrated significant potential in targeted drug delivery,[111,112] particularly due to their ability to be magnetically controlled by an external field to trigger drug release and enhance tumor targeting.[113] Mascolo et al. reported that MNPs synthesized via the coprecipitation method using NaOH as the alkaline solution can achieve a saturation magnetization of 75.3 emu/g.[63] This property is crucial, as nanoparticles with high saturation magnetization can be precisely directed to specific tissues using external magnetic fields, improving the efficiency of therapeutic delivery and reducing off-target effects.[113] Given the promising potential of magnetite nanocarriers, our future work will focus on evaluating the effectiveness of the nanobioconjugates developed in this study using an in vivo murine melanoma model, utilizing magnetic fields to improve tumor targeting.

https://doi.org/10.1021/acsomega.4c07415
ACS Omega 2024, 9, 45402−45420

5. CONCLUSIONS

Our study highlights the potential of MNPs as a promising drug delivery platform for melanoma treatment. By loading these nanoparticles with TMZ and PTX and immobilizing selected molecules, we aimed to achieve passive targeted drug delivery, thereby minimizing off-target effects and maximizing drug accumulation within tumors. Through comprehensive characterization techniques, we confirmed successful synthesis, functionalization, and drug loading, with the nanoparticles' size being optimal for enhanced tumor penetration via the EPR effect. Their biocompatibility, demonstrated by nonhemolytic properties, supports their suitability for intravenous use. Cytotoxicity evaluations revealed that the TMZ and PTX nanobioconjugates were particularly effective against melanoma cells, showing selective cytotoxicity. Cellular internalization studies indicated predominant uptake through endocytic pathways, including caveolae-mediated, clathrin-mediated, and macropinocytosis. The efficacy of these nanobioconjugates was further validated in A-375 spheroid models, exhibiting significant cytotoxic effects. In summary, our findings position these nanobioconjugates as promising platforms for melanoma drug delivery, combining nanotechnology's strengths with passive tumor-specific targeting. Future work will focus on more extensive *in vitro* and *in vivo* evaluations to set these outcomes.

■ ASSOCIATED CONTENT

Supporting Information

The Supporting Information is available free of charge at https://pubs.acs.org/doi/10.1021/acsomega.4c07415.

This document includes materials, methods for physicochemical characterization, nanobioconjugate labeling methodology, and supplementary results such as magnetic response, TEM images, cytotoxicity assays, cellular internalization pathways, and endosomal escape analysis (PDF)

■ AUTHOR INFORMATION

Corresponding Author

Juan C. Cruz − *Department of Biomedical Engineering, Universidad de Los Andes, Bogotá 111711, Colombia;* orcid.org/0000-0002-7790-7546; Phone: +57(601)-3394949; Email: jc.cruz@uniandes.edu.co

Authors

Erika Díaz − *Department of Biomedical Engineering, Universidad de Los Andes, Bogotá 111711, Colombia*

Valentina Quezada − *Department of Biomedical Engineering, Universidad de Los Andes, Bogotá 111711, Colombia*

Javier Cifuentes − *Department of Biomedical Engineering, Universidad de Los Andes, Bogotá 111711, Colombia;* orcid.org/0000-0003-0916-3909

Nydia Yadira Arias Morales − *Center for Microscopy (MicroCore), Vice Presidency for Research and Creation, Universidad de Los Andes, Bogotá 111711, Colombia*

Luis H. Reyes − *Product and Process Design Group (GDPP), Department of Chemical and Food Engineering, Universidad de Los Andes, Bogotá 111711, Colombia;* orcid.org/0000-0001-7251-5298

Carolina Muñoz-Camargo − *Department of Biomedical Engineering, Universidad de Los Andes, Bogotá 111711, Colombia;* orcid.org/0000-0001-6238-9021

Complete contact information is available at: https://pubs.acs.org/10.1021/acsomega.4c07415

Author Contributions

[‖]Co-first author, E.D. and V.Q. contributed equally. Conceptualization, J.C.C., E.D., V.Q., and J.C.; methodology, E.D., V.Q., and J.C.; confocal images acquisition, N.A.; data curation and data analysis E.D. and V.Q.; formal analysis and investigation, E.D. and V.Q.; resources, J.C.C., C.M.-C., and L.H.R.; writing—original draft preparation, E.D. and V.Q.; writing—review and editing, J.C.C.; supervision, J.C.C., C.M.-C., and L.H.R.; funding acquisition, J.C.C., C.M.-C., and L.H.R. All authors have read and agreed to the published version of the manuscript.

Funding

This work was funded by the Colombian Ministry of Science, Technology, and Innovation (Minciencias) Grant Contract # 624-2022, and the School of Engineering grant "Convocatoria para crear nuevos vinculos entre profesoresf-ali-2022".

Notes

The protocols for evaluating the hemolytic capacity and platelet aggregating properties of the developed nanobioconjugates using human blood samples have been reviewed and approved by the Committee of Research Ethics. This approval, documented in minute 928 of the year 2018, was necessary due to the involvement of human participants, specifically the use of blood samples drawn from healthy donors. The Committee of Research Ethics, responsible for overseeing the ethical aspects of research involving human subjects within our institution, provided the necessary clearance for this study. The ethics approval number associated with this study is recorded in minute 928 of 2018, serving as a reference for the specific approval granted. In compliance with ethical research practices and the guidelines set forth by the Committee of Research Ethics, all human participants provided informed consent prior to their participation. Blood samples were obtained only after receiving written informed consent from each donor, ensuring they were fully aware of the study's nature and the use of their blood samples in the research. Study recruitment started on October 12, 2022, and ended on January 8, 2023. Participants provided informed written consent between January 10, 2023, and October 10, 2023.

The authors declare no competing financial interest.

■ ACKNOWLEDGMENTS

The authors acknowledge the instruments and scientific and technical assistance of the MicroCore Microscopy Core at the Universidad de Los Andes, a facility that is supported by the vicepresidency for research and creation.

■ REFERENCES

(1) El-Kenawy, A. E.-M.; Constantin, C.; Hassan, S. M. A.; Mostafa, A. M.; Neves, A. F.; De Araújo, T. G.; Neagu, M. Nanomedicine in Melanoma: Current Trends and Future Perspectives. In *Cutaneous Melanoma: Etiology and Therapy*; Codon Publications, 2017; pp 143−159.

(2) Zeng, H.; Li, J.; Hou, K.; Wu, Y.; Chen, H.; Ning, Z. Melanoma and Nanotechnology-Based Treatment. *Front Oncol.* **2022**, *12*, 858185.

(3) Wilson, B. E.; Jacob, S.; Yap, M. L.; Ferlay, J.; Bray, F.; Barton, M. B. Estimates of Global Chemotherapy Demands and Corresponding Physician Workforce Requirements for 2018 and 2040: A Population-Based Study. *Lancet Oncol.* **2019**, *20* (6), 769−780.

(4) Song, M.; Liu, C.; Chen, S.; Zhang, W. Nanocarrier-Based Drug Delivery for Melanoma Therapeutics. *Int. J. Mol. Sci.* **2021**, *22* (4), 1873.
(5) Yao, Y.; Zhou, Y.; Liu, L.; Xu, Y.; Chen, Q.; Wang, Y.; Wu, S.; Deng, Y.; Zhang, J.; Shao, A. Nanoparticle-Based Drug Delivery in Cancer Therapy and Its Role in Overcoming Drug Resistance. *Front. Mol. Biosci.* **2020**, *7*, 193.
(6) Gavas, S.; Quazi, S.; Karpiński, T. M. Nanoparticles for Cancer Therapy: Current Progress and Challenges. *Nanoscale Res. Lett.* **2021**, *16* (1), 173.
(7) Jin, G.; Cheah, P.; Qu, J.; Liu, L.; Zhao, Y. Applications of Nanomaterials for Theranostics of Melanoma. *J. Nanotheranost.* **2020**, *1* (1), 39−55.
(8) Zhu, L.; Chen, L. Progress in Research on Paclitaxel and Tumor Immunotherapy. *Cell Mol. Biol. Lett.* **2019**, *24* (1), 40.
(9) Wesolowski, J. R.; Rajdev, P.; Mukherji, S. K. Temozolomide (Temodar). *Am. J. Neuroradiol.* **2010**, *31* (8), 1383−1384.
(10) Hu, Y.; Yue, H.; Huang, S.; Song, B.; Xing, Y.; Liu, M.; Wang, G.; Diao, Y.; Zhang, S. Biocompatible Diimidazolium Based Ionic Liquid Systems for Enhancing the Solubility of Paclitaxel. *Green Chem.* **2024**, *26* (7), 4013−4023.
(11) Clemente, N.; Ferrara, B.; Gigliotti, C.; Boggio, E.; Capucchio, M.; Biasibetti, E.; Schiffer, D.; Mellai, M.; Annovazzi, L.; Cangemi, L.; Muntoni, E.; Miglio, G.; Dianzani, U.; Battaglia, L.; Dianzani, C. Solid Lipid Nanoparticles Carrying Temozolomide for Melanoma Treatment. Preliminary In Vitro and In Vivo Studies. *Int. J. Mol. Sci.* **2018**, *19* (2), 255.
(12) Ying, N.; Liu, S.; Zhang, M.; Cheng, J.; Luo, L.; Jiang, J.; Shi, G.; Wu, S.; Ji, J.; Su, H.; Pan, H.; Zeng, D. Nano Delivery System for Paclitaxel: Recent Advances in Cancer Theranostics. *Colloids Surf. B Biointerfaces* **2023**, *228*, No. 113419.
(13) Zhao, J.; Stenzel, M. H. Entry of Nanoparticles into Cells: The Importance of Nanoparticle Properties. *Polym. Chem.* **2018**, *9* (3), 259−272.
(14) Subhan, M. A.; Yalamarty, S. S. K.; Filipczak, N.; Parveen, F.; Torchilin, V. P. Recent Advances in Tumor Targeting via EPR Effect for Cancer Treatment. *J. Pers Med.* **2021**, *11* (6), 571.
(15) Pillai, G. Nanotechnology Toward Treating Cancer. In *Applications of Targeted Nano Drugs and Delivery Systems*; Elsevier, 2019; pp 221−256.
(16) Pavlik, T. I.; Fedotcheva, T. A.; Gusein-zade, N. G.; Shimanovsky, N. L. Combined Effects of Doxorubicin, Medroxyprogesterone Acetate, and Cold-Plasma-Treated Hanks Solution on the Production of Transforming Growth Factor β in Human Mononuclear Leukocytes. *Pharm. Chem. J.* **2022**, *56* (5), 583−586.
(17) Shaw, P.; Vanraes, P.; Kumar, N.; Bogaerts, A. Possible Synergies of Nanomaterial-Assisted Tissue Regeneration in Plasma Medicine: Mechanisms and Safety Concerns. *Nanomaterials* **2022**, *12* (19), 3397.
(18) Revia, R. A.; Zhang, M. Magnetite Nanoparticles for Cancer Diagnosis, Treatment, and Treatment Monitoring: Recent Advances. *Mater. Today* **2016**, *19* (3), 157−168.
(19) Al-husseiny, R. A.; Ebrahim, S. E. Synthesis of Nano-Magnetite and Magnetite/Synthetic Geopolymer Nano-Porous Composite for Application as a Novel Adsorbent. *Environ. Nanotechnol Monit Manag.* **2022**, *18*, No. 100700.
(20) Montazeri, A. R.; Moghimi, H.; Ghourchian, H.; Maghami, P. Characteristics Investigation and Synergistic Anticancer Effects of Immobilized L-Asparaginase onto Iron-Gold Core-Shell Combined with Cold Atmospheric Pressure Plasma. *Process Biochem.* **2023**, *126*, 125−135.
(21) Qi, G.; Wang, S.; Yin, Q.; Zhang, Z.; Wen, X.; Hao, L. A PH-Responsive Nanoplatform Based on Magnetic Mesoporous Silica Nanoparticles for Enhanced Treatment of Pancreatic Cancer. *ACS Appl. Nano Mater.* **2023**, *6* (24), 23184−23195.
(22) Bulatao, B. P.; Nalinratana, N.; Jantaratana, P.; Vajragupta, O.; Rojsitthisak, P.; Rojsitthisak, P. Lutein-Loaded Chitosan/Alginate-Coated Fe3O4 Nanoparticles as Effective Targeted Carriers for Breast Cancer Treatment. *Int. J. Biol. Macromol.* **2023**, *242*, No. 124673.
(23) Zhou, X.; He, X.; Dong, Z.; Wang, Y.; Hu, C.; Zhang, D.; Guo, R.; Qiao, J.; Li, N. Manganese-Doped Mesoporous Magnetic Nanocarriers for Cancer Treatment. *ACS Appl. Nano Mater.* **2024**, *7* (6), 6339−6350.
(24) Cardellini, J.; Surpi, A.; Muzzi, B.; Pacciani, V.; Innocenti, C.; Sangregorio, C.; Dediu, V. A.; Montis, C.; Berti, D. Magnetic−Plasmonic Nanoscale Liposomes with Tunable Optical and Magnetic Properties for Combined Multimodal Imaging and Drug Delivery. *ACS Appl. Nano Mater.* **2024**, *7* (4), 3668−3678.
(25) Jiang, G.; Li, R.; Tang, J.; Ma, Y.; Hou, X.; Yang, C.; Guo, W.; Xin, Y.; Liu, Y. Formulation of Temozolomide-Loaded Nanoparticles and Their Targeting Potential to Melanoma Cells. *Oncol. Rep.* **2017**, *37* (2), 995−1001.
(26) Moghaddam, A. S.; Khonakdar, H. A.; Sarikhani, E.; Jafari, S. H.; Javadi, A.; Shamsi, M.; Amirkhani, M. A.; Ahadian, S. Fabrication of Carboxymethyl Chitosan Nanoparticles to Deliver Paclitaxel for Melanoma Treatment. *ChemNanoMat* **2020**, *6* (9), 1373−1385.
(27) Oliveira, R. R.; Cintra, E. R.; Sousa-Junior, A. A.; Moreira, L. C.; da Silva, A. C. G.; de Souza, A. L. R.; Valadares, M. C.; Carrião, M. S.; Bakuzis, A. F.; Lima, E. M. Paclitaxel-Loaded Lipid-Coated Magnetic Nanoparticles for Dual Chemo-Magnetic Hyperthermia Therapy of Melanoma. *Pharmaceutics* **2023**, *15* (3), 818.
(28) Aslibeiki, B.; Eskandarzadeh, N.; Jalili, H.; Ghotbi Varzaneh, A.; Kameli, P.; Orue, I.; Chernenko, V.; Hajalilou, A.; Ferreira, L. P.; Cruz, M. M. Magnetic Hyperthermia Properties of CoFe2O4 Nanoparticles: Effect of Polymer Coating and Interparticle Interactions. *Ceram. Int.* **2022**, *48* (19), 27995−28005.
(29) Al-Obaidy, R.; Haider, A. J.; Al-Musawi, S.; Arsad, N. Targeted Delivery of Paclitaxel Drug Using Polymer-Coated Magnetic Nanoparticles for Fibrosarcoma Therapy: In Vitro and in Vivo Studies. *Sci. Rep.* **2023**, *13* (1), No. 3180.
(30) Hou, X.; Pang, Y.; Li, X.; Yang, C.; Liu, W.; Jiang, G.; Liu, Y. Core-shell Type Thermo-nanoparticles Loaded with Temozolomide Combined with Photothermal Therapy in Melanoma Cells. *Oncol. Rep.* **2019**, 2512.
(31) Tang, J.; Zhou, H.; Hou, X.; Wang, L.; Li, Y.; Pang, Y.; Chen, C.; Jiang, G.; Liu, Y. Enhanced Anti-Tumor Efficacy of Temozolomide-Loaded Carboxylated Poly(Amido-Amine) Combined with Photothermal/Photodynamic Therapy for Melanoma Treatment. *Cancer Lett.* **2018**, *423*, 16−26.
(32) Ganapathe, L. S.; Mohamed, M. A.; Mohamad Yunus, R.; Berhanuddin, D. D. Magnetite (Fe3O4) Nanoparticles in Biomedical Application: From Synthesis to Surface Functionalisation. *Magnetochemistry* **2020**, *6* (4), 68.
(33) Ghazanfari, M. R.; Kashefi, M.; Shams, S. F.; Jaafari, M. R. Perspective of Fe3O4 Nanoparticles Role in Biomedical Applications. *Biochem Res. Int.* **2016**, *2016*, 1−32.
(34) Petcharoen, K.; Sirivat, A. Synthesis and Characterization of Magnetite Nanoparticles via the Chemical Co-Precipitation Method. *Mater. Sci. Eng.: B* **2012**, *177* (5), 421−427.
(35) Ahn, T.; Kim, J. H.; Yang, H.-M.; Lee, J. W.; Kim, J.-D. Formation Pathways of Magnetite Nanoparticles by Coprecipitation Method. *J. Phys. Chem. C* **2012**, *116* (10), 6069−6076.
(36) Shan, X.; Yuan, Y.; Liu, C.; Tao, X.; Sheng, Y.; Xu, F. Influence of PEG Chain on the Complement Activation Suppression and Longevity in Vivo Prolongation of the PCL Biomedical Nanoparticles. *Biomed. Microdevices* **2009**, *11* (6), 1187−1194.
(37) Karakoti, A. S.; Das, S.; Thevuthasan, S.; Seal, S. PEGylated Inorganic Nanoparticles. *Angew. Chem., Int. Ed.* **2011**, *50* (9), 1980−1994.
(38) Hervé, K.; Douziech-Eyrolles, L.; Munnier, E.; Cohen-Jonathan, S.; Soucé, M.; Marchais, H.; Limelette, P.; Warmont, F.; Saboungi, M. L.; Dubois, P.; Chourpa, I. The Development of Stable Aqueous Suspensions of PEGylated SPIONs for Biomedical Applications. *Nanotechnology* **2008**, *19* (46), No. 465608.
(39) Lankveld, D. P.; Rayavarapu, R. G.; Krystek, P.; Oomen, A. G.; Verharen, H. W.; van Leeuwen, T. G.; De Jong, W. H.; Manohar, S. Blood Clearance and Tissue Distribution of PEGylated and Non-

https://doi.org/10.1021/acsomega.4c07415
ACS Omega 2024, 9, 45402−45420

PEGylated Gold Nanorods after Intravenous Administration in Rats. *Nanomedicine* **2011**, *6* (2), 339−349.
(40) Kobayashi, S.; Chikushi, A.; Tougu, S.; Imura, Y.; Nishida, M.; Yano, Y.; Matsuzaki, K. Membrane Translocation Mechanism of the Antimicrobial Peptide Buforin 2. *Biochemistry* **2004**, *43* (49), 15610−15616.
(41) Tolos (Vasii), A. M.; Moisa, C.; Dochia, M.; Popa, C.; Copolovici, L.; Copolovici, D. M. Anticancer Potential of Antimicrobial Peptides: Focus on Buforins. *Polymers* **2024**, *16* (6), 728.
(42) Roudi, R.; Syn, N. L.; Roudbary, M. Antimicrobial Peptides As Biologic and Immunotherapeutic Agents against Cancer: A Comprehensive Overview. *Front. Immunol.* **2017**, *8*, 1320 DOI: 10.3389/fimmu.2017.01320.
(43) Perez, J.; Rueda, J.; Cuellar, M.; Suarez-Arnedo, A.; Cruz, J. C.; Muñoz-Camargo, C. Cell-Penetrating and Antibacterial BUF-II Nanobioconjugates: Enhanced Potency Via Immobilization On Polyetheramine-Modified Magnetite Nanoparticles. *Int. J. Nanomed.* **2019**, *14*, 8483−8497.
(44) Cuellar, M.; Cifuentes, J.; Perez, J.; Suarez-Arnedo, A.; Serna, J.; Groot, H.; Muñoz-Camargo, C.; Cruz, J. Novel BUF2-Magnetite Nanobioconjugates with Cell-Penetrating Abilities. *Int. J. Nanomed.* **2018**, *13*, 8087−8094.
(45) Arango, D.; Cifuentes, J.; Puentes, P. R.; Beltran, T.; Bittar, A.; Ocasión, C.; Muñoz-Camargo, C.; Bloch, N. I.; Reyes, L. H.; Cruz, J. C. Tailoring Magnetite-Nanoparticle-Based Nanocarriers for Gene Delivery: Exploiting CRISPRa Potential in Reducing Conditions. *Nanomaterials* **2023**, *13* (11), 1782.
(46) Torres-Vanegas, J. D.; Cifuentes, J.; Puentes, P. R.; Quezada, V.; Garcia-Brand, A. J.; Cruz, J. C.; Reyes, L. H. Assessing Cellular Internalization and Endosomal Escape Abilities of Novel BUFII-Graphene Oxide Nanobioconjugates. *Front Chem.* **2022**, *10*, 974218.
(47) Almaghrabi, M.; Alqurshi, A.; Jadhav, S. A.; Mazzacuva, F.; Cilibrizzi, A.; Raimi-Abraham, B.; Royall, P. G. Evaluating Thermogravimetric Analysis for the Measurement of Drug Loading in Mesoporous Silica Nanoparticles (MSNs). *Thermochim. Acta* **2023**, *730*, No. 179616.
(48) Nagai, N.; Ogata, F.; Ishii, M.; Fukuoka, Y.; Otake, H.; Nakazawa, Y.; Kawasaki, N. Involvement of Endocytosis in the Transdermal Penetration Mechanism of Ketoprofen Nanoparticles. *Int. J. Mol. Sci.* **2018**, *19* (7), 2138.
(49) Xia, H.; Huang, Y.; Zhang, L.; Luo, L.; Wang, X.; Lu, Q.; Xu, J.; Yang, C.; Jiwa, H.; Liang, S.; Xie, L.; Luo, X.; Luo, J. Inhibition of Macropinocytosis Enhances the Sensitivity of Osteosarcoma Cells to Benzethonium Chloride. *Cancers* **2023**, *15* (3), 961.
(50) Sun, S.-w.; Zu, X.; Tuo, Q.; Chen, L.; Lei, X.; Li, K.; Tang, C.; Liao, D. Caveolae and Caveolin-1 Mediate Endocytosis and Transcytosis of Oxidized Low Density Lipoprotein in Endothelial Cells. *Acta Pharmacol Sin* **2010**, *31* (10), 1336−1342.
(51) Kirchhausen, T.; Macia, E.; Pelish, H. E. Use of Dynasore, the Small Molecule Inhibitor of Dynamin, in the Regulation of Endocytosis. *Methods Enzymol.* **2008**, *438*, 77−93.
(52) Ramírez-Acosta, C. M.; Cifuentes, J.; Castellanos, M. C.; Moreno, R. J.; Muñoz-Camargo, C.; Cruz, J. C.; Reyes, L. H. PH-Responsive, Cell-Penetrating, Core/Shell Magnetite/Silver Nanoparticles for the Delivery of Plasmids: Preparation, Characterization, and Preliminary In Vitro Evaluation. *Pharmaceutics* **2020**, *12* (6), 561.
(53) Muñoz, L. N.; Jaramillo, V.; Gantiva-Diaz, M.; Cifuentes, J.; Muñoz-Camargo, C.; Cruz, J. C.; González Barrios, A. F. Formulation of a Novel Antibacterial Topical Treatment Based on Magnetite-Buforin-II-Silver Nanobioconjugates. *Front. Bioeng. Biotechnol.* **2022**, *10*, 1003004.
(54) Martinho, O.; Vilaça, N.; Castro, P. J. G.; Amorim, R.; Fonseca, A. M.; Baltazar, F.; Reis, R. M.; Neves, I. C. In Vitro and in Vivo Studies of Temozolomide Loading in Zeolite Structures as Drug Delivery Systems for Glioblastoma. *RSC Adv.* **2015**, *5* (36), 28219−28227.
(55) Kadhim, Z. A.; Sulaiman, G. M.; Al-Shammari, A. M.; Khan, R. A.; Al Rugaie, O.; Mohammed, H. A. Oncolytic Newcastle Disease Virus Co-Delivered with Modified PLGA Nanoparticles Encapsulating Temozolomide against Glioblastoma Cells: Developing an Effective Treatment Strategy. *Molecules* **2022**, *27* (18), 5757.
(56) Hiremath, J. G.; Khamar, N. S.; Palavalli, S. G.; Rudani, C. G.; Aitha, R.; Mura, P. Paclitaxel Loaded Carrier Based Biodegradable Polymeric Implants: Preparation and in Vitro Characterization. *Saudi Pharm. J.* **2013**, *21* (1), 85−91.
(57) Ha, P. T.; Nguyen, H. N.; Do, H. D.; Phan, Q. T.; Thi, M. N. T.; Nguyen, X. P.; Thi, M. N. H.; Le, M. H.; Nguyen, L. T.; Bui, T. Q.; Phan, V. H. Targeted Drug Delivery Nanosystems Based on Copolymer Poly(Lactide)-Tocopheryl Polyethylene Glycol Succinate for Cancer Treatment. *Adv. Nat. Sci.: Nanosci. Nanotechnol.* **2016**, *7* (1), No. 015001.
(58) Cifuentes, J.; Cifuentes-Almanza, S.; Ruiz Puentes, P.; Quezada, V.; González Barrios, A. F.; Calderón-Peláez, M.-A.; Velandia-Romero, M. L.; Rafat, M.; Muñoz-Camargo, C.; Albarracín, S. L.; Cruz, J. C. Multifunctional Magnetoliposomes as Drug Delivery Vehicles for the Potential Treatment of Parkinson's Disease. *Front Bioeng Biotechnol* **2023**, *11*, 1181842.
(59) Lopez-Barbosa, N.; Suárez-Arnedo, A.; Cifuentes, J.; Gonzalez Barrios, A. F.; Silvera Batista, C. A.; Osma, J. F.; Muñoz-Camargo, C.; Cruz, J. C. Magnetite−OmpA Nanobioconjugates as Cell-Penetrating Vehicles with Endosomal Escape Abilities. *ACS Biomater. Sci. Eng.* **2020**, *6* (1), 415−424.
(60) Rizvi, S. A. A.; Saleh, A. M. Applications of Nanoparticle Systems in Drug Delivery Technology. *Saudi Pharm. J.* **2018**, *26* (1), 64−70.
(61) Islam, M. A.; Barua, S.; Barua, D. A Multiscale Modeling Study of Particle Size Effects on the Tissue Penetration Efficacy of Drug-Delivery Nanoparticles. *BMC Syst. Biol.* **2017**, *11* (1), 113.
(62) Maity, D.; Agrawal, D. C. Synthesis of Iron Oxide Nanoparticles under Oxidizing Environment and Their Stabilization in Aqueous and Non-Aqueous Media. *J. Magn Magn. Mater.* **2007**, *308* (1), 46−55.
(63) Mascolo, M.; Pei, Y.; Ring, T. Room Temperature Co-Precipitation Synthesis of Magnetite Nanoparticles in a Large PH Window with Different Bases. *Materials* **2013**, *6* (12), 5549−5567.
(64) Meylina, L.; Muchtaridi, M.; Joni, I. M.; Mohammed, A. F. A.; Wathoni, N. Nanoformulations of α-Mangostin for Cancer Drug Delivery System. *Pharmaceutics* **2021**, *13* (12), 1993.
(65) Torres, C. E.; Cifuentes, J.; Gómez, S. C.; Quezada, V.; Giraldo, K. A.; Puentes, P. R.; Rueda-Gensini, L.; Serna, J. A.; Muñoz-Camargo, C.; Reyes, L. H.; Osma, J. F.; Cruz, J. C. Microfluidic Synthesis and Purification of Magnetoliposomes for Potential Applications in the Gastrointestinal Delivery of Difficult-to-Transport Drugs. *Pharmaceutics* **2022**, *14* (2), 315.
(66) Kędzierska, M.; Potemski, P.; Drabczyk, A.; Kudłacik-Kramarczyk, S.; Głąb, M.; Grabowska, B.; Mierzwiński, D.; Tyliszczak, B. The Synthesis Methodology of PEGylated Fe3O4@Ag Nanoparticles Supported by Their Physicochemical Evaluation. *Molecules* **2021**, *26* (6), 1744.
(67) Akl, M. A.; Atta, A. M.; Yousef, A. E.-F. M.; Alaa, M. I. Characterization of Stabilized Porous Magnetite Core-Shell Nanogel Composites Based on Crosslinked Acrylamide/Sodium Acrylate Copolymers. *Polym. Int.* **2013**, *62* (12), 1667−1677.
(68) Illés, E.; Tombácz, E.; Szekeres, M.; Tóth, I. Y.; Szabó, Á.; Iván, B. Novel Carboxylated PEG-Coating on Magnetite Nanoparticles Designed for Biomedical Applications. *J. Magn. Magn. Mater.* **2015**, *380*, 132−139.
(69) Zhang, J.; Lin, S.; Han, M.; Su, Q.; Xia, L.; Hui, Z. Adsorption Properties of Magnetic Magnetite Nanoparticle for Coexistent Cr(VI) and Cu(II) in Mixed Solution. *Water* **2020**, *12* (2), 446.
(70) Lee, J.-M.; Lim, D.-S.; Jeon, S.-H.; Hur, D. H. Zeta Potentials of Magnetite Particles and Alloy 690 Surfaces in Alkaline Solutions. *Materials* **2020**, *13* (18), 3999.
(71) Ravelo-Nieto, E.; Cifuentes, J.; Ruiz Puentes, P.; Rueda-Gensini, L.; Quezada, V.; Ostos, C.; Muñoz-Camargo, C.; Reyes, L. H.; Duarte-Ruiz, A.; Cruz, J. C. Unlocking Cellular Barriers: Silica Nanoparticles and Fullerenol Conjugated Cell-Penetrating Agents for

https://doi.org/10.1021/acsomega.4c07415
ACS Omega 2024, 9, 45402−45420

Enhanced Intracellular Drug Delivery. *Front. Bioeng. Biotechnol.* **2023**, *11*, 1184973.
(72) Minaei, S. E.; Khoei, S.; Khoee, S.; Vafashoar, F.; Mahabadi, V. P. In Vitro Anti-Cancer Efficacy of Multi-Functionalized Magnetite Nanoparticles Combining Alternating Magnetic Hyperthermia in Glioblastoma Cancer Cells. *Mater. Sci. Eng.: C* **2019**, *101*, 575−587.
(73) Sakhi, M.; Khan, A.; Iqbal, Z.; Khan, I.; Raza, A.; Ullah, A.; Nasir, F.; Khan, S. A. Design and Characterization of Paclitaxel-Loaded Polymeric Nanoparticles Decorated With Trastuzumab for the Effective Treatment of Breast Cancer. *Front. Pharmacol.* **2022**, *13*, 855294.
(74) Ganipineni, L. P.; Ucakar, B.; Joudiou, N.; Bianco, J.; Danhier, P.; Zhao, M.; Bastiancich, C.; Gallez, B.; Danhier, F.; Préat, V. Magnetic Targeting of Paclitaxel-Loaded Poly(Lactic-Co-Glycolic Acid)-Based Nanoparticles for the Treatment of Glioblastoma. *Int. J. Nanomed.* **2018**, *13*, 4509−4521.
(75) Rueda-Gensini, L.; Cifuentes, J.; Castellanos, M. C.; Puentes, P. R.; Serna, J. A.; Muñoz-Camargo, C.; Cruz, J. C. Tailoring Iron Oxide Nanoparticles for Efficient Cellular Internalization and Endosomal Escape. *Nanomaterials* **2020**, *10* (9), 1816.
(76) Wei, Y.; Tang, T.; Pang, H.-B. Cellular Internalization of Bystander Nanomaterial Induced by TAT-Nanoparticles and Regulated by Extracellular Cysteine. *Nat. Commun.* **2019**, *10* (1), No. 3646.
(77) Motta, S.; Siani, P.; Levy, A.; Di Valentin, C. Exploring the Drug Loading Mechanism of Photoactive Inorganic Nanocarriers through Molecular Dynamics Simulations. *Nanoscale* **2021**, *13* (30), 13000−13013.
(78) Mahdavi, M.; Fattahi, A.; Tajkhorshid, E.; Nouranian, S. Molecular Insights into the Loading and Dynamics of Doxorubicin on PEGylated Graphene Oxide Nanocarriers. *ACS Appl. Bio Mater.* **2020**, *3* (3), 1354−1363.
(79) Li, Y.; Yang, L. Driving Forces for Drug Loading in Drug Carriers. *J. Microencapsul.* **2015**, *32* (3), 255−272.
(80) Honary, S.; Zahir, F. Effect of Zeta Potential on the Properties of Nano-Drug Delivery Systems - A Review (Part 1). *Tropical J. Pharmaceut. Res.* **2013**, *12* (2), 255.
(81) Ran, S.; Downes, A.; Thorpe, P. E. Increased Exposure of Anionic Phospholipids on the Surface of Tumor Blood Vessels. *Cancer Res.* **2002**, *62* (21), 6132−6140.
(82) Lee, E. Polymeric Micelle for Tumor PH and Folate-Mediated Targeting. *J. Controlled Release* **2003**, *91* (1−2), 103−113.
(83) Mahoney, B. P.; Raghunand, N.; Baggett, B.; Gillies, R. J. Tumor Acidity, Ion Trapping and Chemotherapeutics. *Biochem. Pharmacol.* **2003**, *66* (7), 1207−1218.
(84) Garcia-Martin, M. L.; Martinez, G. V.; Raghunand, N.; Sherry, A. D.; Zhang, S.; Gillies, R. J. High Resolution PH(e) Imaging of Rat Glioma Using PH-dependent Relaxivity. *Magn. Reson. Med.* **2006**, *55* (2), 309−315.
(85) Sun, B.; Wu, W.; Narasipura, E. A.; Ma, Y.; Yu, C.; Fenton, O. S.; Song, H. Engineering Nanoparticle Toolkits for MRNA Delivery. *Adv. Drug Delivery Rev.* **2023**, *200*, No. 115042.
(86) Meng, C.; Chen, Z.; Li, G.; Welte, T.; Shen, H. Nanoplatforms for MRNA Therapeutics. *Adv. Ther.* **2021**, *4* (1), 2000099.
(87) Lee, H. S.; Park, C. B.; Kim, J. M.; Jang, S. A.; Park, I. Y.; Kim, M. S.; Cho, J. H.; Kim, S. C. Mechanism of Anticancer Activity of Buforin IIb, a Histone H2A-Derived Peptide. *Cancer Lett.* **2008**, *271* (1), 47−55.
(88) Han, Y.; Lu, M.; Zhou, J. Buforin IIb Induces Androgen-Independent Prostate Cancer Cells Apoptosis Though P53 Pathway in Vitro. *Toxicon* **2019**, *168*, 16−21.
(89) Jang, J. H.; Kim, M. Y.; Lee, J.-W.; Kim, S. C.; Cho, J. H. Enhancement of the Cancer Targeting Specificity of Buforin IIb by Fusion with an Anionic Peptide via a Matrix Metalloproteinases-Cleavable Linker. *Peptides* **2011**, *32* (5), 895−899.
(90) Hiremath, C. G.; Heggnnavar, G. B.; Kariduraganavar, M. Y.; Hiremath, M. B. Co-Delivery of Paclitaxel and Curcumin to Foliate Positive Cancer Cells Using Pluronic-Coated Iron Oxide Nanoparticles. *Prog. Biomater.* **2019**, *8* (3), 155−168.
(91) Wong, P. T.; Choi, S. K. Mechanisms of Drug Release in Nanotherapeutic Delivery Systems. *Chem. Rev.* **2015**, *115* (9), 3388−3432.
(92) Da, X.; Li, R.; Li, X.; Lu, Y.; Gu, F.; Liu, Y. Synthesis and Characterization of PEG Coated Hollow Fe3O4Magnetic Nanoparticles as a Drug Carrier. *Mater. Lett.* **2022**, *309*, No. 131357.
(93) Sanchez Armengol, E.; Unterweger, A.; Laffleur, F. PEGylated Drug Delivery Systems in the Pharmaceutical Field: Past, Present and Future Perspective. *Drug Dev. Ind. Pharm.* **2022**, *48* (4), 129−139.
(94) Suk, J. S.; Xu, Q.; Kim, N.; Hanes, J.; Ensign, L. M. PEGylation as a Strategy for Improving Nanoparticle-Based Drug and Gene Delivery. *Adv. Drug Delivery Rev.* **2016**, *99*, 28−51.
(95) Roy, H. K.; DiBaise, J. K.; Black, J.; Karolski, W. J.; Ratashak, A.; Ansari, S. Polyethylene Glycol Induces Apoptosis in HT-29 Cells: Potential Mechanism for Chemoprevention of Colon Cancer. *FEBS Lett.* **2001**, *496* (2−3), 143−146.
(96) Wali, R. K.; Kunte, D. P.; Koetsier, J. L.; Bissonnette, M.; Roy, H. K. Polyethylene Glycol-Mediated Colorectal Cancer Chemoprevention: Roles of Epidermal Growth Factor Receptor and Snail. *Mol. Cancer Ther.* **2008**, *7* (9), 3103−3111.
(97) Hugger, E. D.; Audus, K. L.; Borchardt, R. T. Effects of Poly(Ethylene Glycol) on Efflux Transporter Activity in Caco-2 Cell Monolayers. *J. Pharm. Sci.* **2002**, *91* (9), 1980−1990.
(98) Johnson, B. M.; Charman, W. N.; Porter, C. J. H. An in Vitro Examination of the Impact of Polyethylene Glycol 400, Pluronic P85, and Vitamin E d-a-Tocopheryl Polyethylene Glycol 1000 Succinate on P-Glycoprotein Efflux and Enterocyte-Based Metabolism in Excised Rat Intestine. *AAPS PharmSci.* **2002**, *4* (4), 193−205.
(99) Postic, I.; Sheardown, H. Poly(Ethylene Glycol) Induces Cell Toxicity in Melanoma Cells by Producing a Hyperosmotic Extracellular Medium. *J. Biomater Appl.* **2018**, *33* (5), 693−706.
(100) Reifarth, M.; Hoeppener, S.; Schubert, U. S. Uptake and Intracellular Fate of Engineered Nanoparticles in Mammalian Cells: Capabilities and Limitations of Transmission Electron Microscopy—Polymer-Based Nanoparticles. *Adv. Mater.* **2018**, *30* (9), 1703704.
(101) Zhang, L.; Tian, X. Y.; Chan, C. K. W.; Bai, Q.; Cheng, C. K.; Chen, F. M.; Cheung, M. S. H.; Yin, B.; Yang, H.; Yung, W.-Y.; Chen, Z.; Ding, F.; Leung, K. C.-F.; Zhang, C.; Huang, Y.; Lau, J. Y. W.; Choi, C. H. J. Promoting the Delivery of Nanoparticles to Atherosclerotic Plaques by DNA Coating. *ACS Appl. Mater. Interfaces* **2019**, *11* (15), 13888−13904.
(102) Bohmer, N.; Jordan, A. Caveolin-1 and CDC42 Mediated Endocytosis of Silica-Coated Iron Oxide Nanoparticles in HeLa Cells. *Beilstein J. Nanotechnol.* **2015**, *6*, 167−176.
(103) Doherty, G. J.; McMahon, H. T. Mechanisms of Endocytosis. *Annu. Rev. Biochem.* **2009**, *78* (1), 857−902.
(104) Poller, W. C.; Ramberger, E.; Boehm-Sturm, P.; Mueller, S.; Möller, K.; Löwa, N.; Wiekhorst, F.; Wagner, S.; Taupitz, M.; Schellenberger, E.; Baumann, G.; Stangl, K.; Stangl, V.; Ludwig, A. Uptake of Citrate-Coated Iron Oxide Nanoparticles into Atherosclerotic Lesions in Mice Occurs via Accelerated Transcytosis through Plaque Endothelial Cells. *Nano Res.* **2016**, *9* (11), 3437−3452.
(105) Chaves, N.; Estrela-Lopis, I.; Böttner, J.; Lopes, C. A. P.; Cândido Guido, B.; Souza, A.; Bao, S. Exploring Cellular Uptake of Iron Oxide Nanoparticles Associated with Rhodium Citrate in Breast Cancer Cells. *Int. J. Nanomed.* **2017**, *Volume 12*, 5511−5523.
(106) Zhou, G.; Zhang, J.; Pan, C.; Liu, N.; Wang, Z.; Zhang, J. Enhanced Uptake of Fe3O4 Nanoparticles by Intestinal Epithelial Cells in a State of Inflammation. *Molecules* **2017**, *22* (8), 1240.
(107) Tang, T.; Valenzuela, A.; Petit, F.; Chow, S.; Leung, K.; Gorin, F.; Louie, A. Y.; Dhenain, M. In Vivo MRI of Functionalized Iron Oxide Nanoparticles for Brain Inflammation. *Contrast Media Mol. Imaging* **2018**, *2018*, 1−10.
(108) Wang, B.; Zhang, L.; Bae, S. C.; Granick, S. Nanoparticle-Induced Surface Reconstruction of Phospholipid Membranes. *Proc. Natl. Acad. Sci. U. S. A.* **2008**, *105* (47), 18171−18175.
(109) Feng, Q.; Liu, Y.; Huang, J.; Chen, K.; Huang, J.; Xiao, K. Uptake, Distribution, Clearance, and Toxicity of Iron Oxide

https://doi.org/10.1021/acsomega.4c07415
ACS Omega 2024, 9, 45402−45420

Nanoparticles with Different Sizes and Coatings. *Sci. Rep.* **2018**, *8* (1), No. 2082.
(110) Nowak-Jary, J.; Machnicka, B. In Vivo Biodistribution and Clearance of Magnetic Iron Oxide Nanoparticles for Medical Applications. *Int. J. Nanomed.* **2023**, *Volume 18*, 4067−4100.
(111) Prijic, S.; Sersa, G. Magnetic Nanoparticles as Targeted Delivery Systems in Oncology. *Radiol. Oncol.* **2011**, *45* (1), 1−16.
(112) kianfar, E. Magnetic Nanoparticles in Targeted Drug Delivery: A Review. *J. Supercond. Nov. Magn.* **2021**, *34* (7), 1709−1735.
(113) Liu, J. F.; Jang, B.; Issadore, D.; Tsourkas, A. Use of Magnetic Fields and Nanoparticles to Trigger Drug Release and Improve Tumor Targeting. *WIREs Nanomed. Nanobiotechnol.* **2019**, *11* (6), e1571.

https://doi.org/10.1021/acsomega.4c07415
ACS Omega 2024, 9, 45402−45420